Ocean Modelling 99 (2016) 43–59

Contents lists available at ScienceDirect

Ocean Modelling

journal homepage: www.elsevier.com/locate/ocemod

# An assessment of the added value from data assimilation on modelled Nordic Seas hydrography and ocean transports

Vidar S. Lien[a,*], Solfrid S. Hjøllo[a], Morten D. Skogen[a], Einar Svendsen[a], Henning Wehde[a], Laurent Bertino[b], Francois Counillon[b], Matthieu Chevallier[c], Gilles Garric[d]

[a] Institute of Marine Research, Pb.1870, N-5817 Bergen, Norway
[b] Nansen Environmental and Remote Sensing Center, Thormøhlens gate 47, N-5006 Bergen, Norway
[c] CNRM/GAME, Météo-France/CNRS UMR 3589, 42 avenue G. Coriolis, 31057 Toulouse, France
[d] Mercator Océan, 8-10 rue Hermès, Parc Technologique du Canal, 31520 Ramonville Saint Agne, France

ARTICLE INFO

*Article history:*
Received 8 June 2015
Revised 21 December 2015
Accepted 27 December 2015
Available online 4 January 2016

*Keywords:*
Ocean modelling
Ocean reanalysis
Atlantic Water
Model comparison
Volume transport
Norwegian Sea

ABSTRACT

The Nordic Seas is a hotspot both in terms of climate related processes, such as Atlantic–Arctic heat exchange, and natural marine resources. A sustainable management of the marine resources within the Nordic Seas, including the co-existence between fisheries and petroleum industries, requires detailed information on the state of the ocean within an operational framework and beyond what is obtainable from observations only. Numerical ocean models applying data assimilation techniques are utilized to address this need. Subsequently, comprehensive comparisons between model results and observations are required in order to assess the model performance. Here, we apply a set of objective statistics to quantitatively assess the added value of data assimilation in numerical ocean models that are currently used operationally. The results indicate that the inclusion of data assimilation improves the model performance both in terms of hydrographic properties and volume and heat transports. Furthermore, we find that increasing the resolution towards eddy resolving resolution performs similarly to coarser resolution models applying data assimilation in shelf areas.



## 1. Introduction

The Nordic Seas, which consists of the Norwegian, Greenland and Iceland seas, together with the Barents Sea constitute the link between the Atlantic and Arctic oceans and accounts for the major part of the heat exchange between the two oceans. This is reflected in the warm and saline Atlantic Water (AW) that looses large amounts of heat as it flows northward along the Nordic Seas eastern boundary, and the cold and relatively fresh Polar Water flowing southward along the Nordic Seas western boundary (Blindheim and Østerhus, 2003; Fig. 1). The Nordic Seas is therefore a hotspot in the northern hemisphere climate system, and has deservedly received a lot of attention in terms of climate related research (e.g., Mauritzen et al., 2011; Smedsrud et al., 2013; Eldevik and Nilsen, 2013; Gerber et al., 2014). Adding to that, the Nordic Seas holds vast amounts of natural resources, such as large commercial fish stocks and fossil fuel reserves. Examples include the world's largest commercial cod stock, the Northeast Arctic cod (*Gadus morhua*), and the Norwegian spring-spawning herring (*Clupea harengus*). The variability in the key marine ecosystem components are closely connected to circulation variability; e.g., fish recruitment in the Barents Sea is positively correlated with inflow of AW from the Norwegian Sea with high abundance of the key zooplankton species *Calanus finmarchicus,* (Sundby, 2000; Ottersen et al., 2013), while reduced inflow of AW has been suggested as a prime candidate for the poor fish recruitment in the North Sea in recent years (Beaugrand et al 2009; Payne et al 2009). Offshore installations at the sea surface related to the fossil fuel industry are prone to physical stress from ocean waves and currents, and as the industry moves further north, sea ice becomes an increasing concern. Moreover, the co-existence between offshore industry and fisheries requires robust assessments of potential environmental impacts of, e.g., oil spills (Hauge et al., 2014).

Detailed information on the state of the ocean beyond what is obtainable from observations only, as well as an understanding of the governing physical processes within the Nordic Seas is needed to address the challenges listed above. In order to provide information on the ocean state operationally, which requires assimilation of observational data into numerical ocean models, the MyOcean projects and follow-on Copernicus Marine Environmental

* Corresponding author. Tel.: +47 41 61 42 80.
*E-mail address:* vidar.lien@imr.no (V.S. Lien).

http://dx.doi.org/10.1016/j.ocemod.2015.12.010

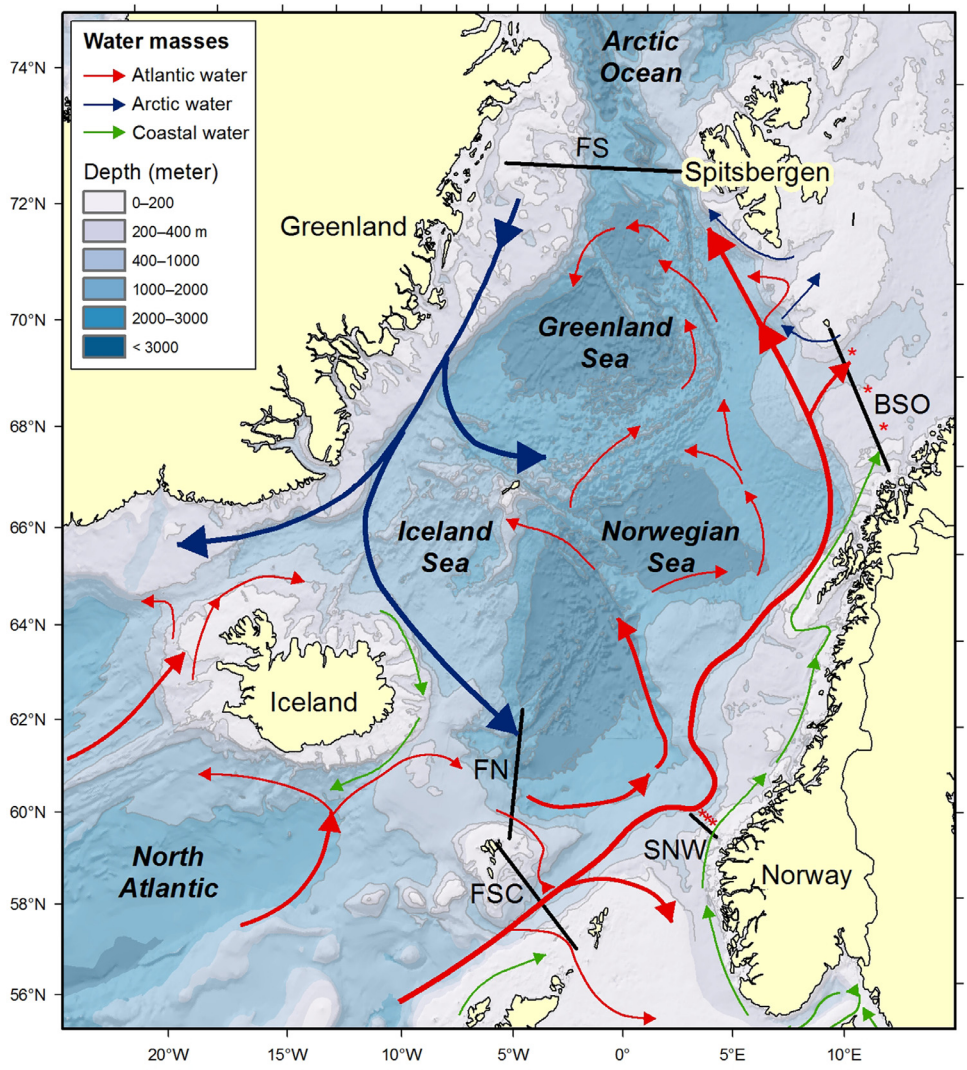


**Fig. 1.** Bathymetry and general circulation in the study area Blue: Arctic water masses; red: Atlantic water masses; green: coastal water masses. Black lines show the positions of the sections; FN = Færøy North, FSC = Færøy–Shetland Channel, SNW = Svinøy Northwest, BSO = Barents Sea Opening, FS = Fram Strait. Red stars show positions of stations with vertical profiles of temperature and salinity. (For interpretation of the references to colour in this figure legend, the reader is referred to the web version of this article.)

Monitoring Service (CMEMS; http://marine.copernicus.eu/) operates and delivers a comprehensive Ocean Monitoring and Forecasting system of the Global Monitoring for Environment and Security program Marine Service to users within all marine applications, including maritime safety, marine resources, marine and coastal environment and climate, seasonal and weather forecasting. At present, two models that cover the Nordic Seas and the Arctic Ocean are run in parallel within the CMEMS framework: the Mercator Océan global system, France (NEMO) and the TOPAZ model system, developed at the Nansen Environmental and Remote Sensing Center, Norway, and run operationally at the Meteorological Institute, Norway.

Several challenges arise when modelling the Nordic Seas. First and foremost, the dynamical length scale represented by the Rossby radius of deformation, which is between 1 and 10 km within the Nordic Seas (Nurser and Bacon, 2014), together with strong hydrographic gradients, often in conjunction with steep topography, put strong constraints on the spatial resolution and the choice of sub-gridscale mixing parameterization required to adequately resolve important processes. Adding to that, the area of the Nordic Seas together with the need of adequately including the boundary areas towards the northern North Atlantic and the Arctic Ocean within the model domain, limits the spatial resolution due to the computational demand, especially within an operational framework. Other complicating factors include, among others, large ocean-atmosphere heat exchange associated with vigorous atmosphere dynamics (e.g., Ivanov and Shapiro, 2005; Segtnan et al., 2011), as well as sea–ice–atmosphere interactions (e.g., Smedsrud et al., 2013). In addition, the data assimilation itself adds challenges related to the freshwater balance and dynamical consistency, among other things.

Our analysis includes assimilation and non-assimilation experiments performed by the two CMEMS models, as well as a non-assimilation mode only simulation using the Regional Ocean Modeling System (ROMS). ROMS is currently used operationally at the Norwegian met office and served as a backup system within the MyOcean projects, i.e., the pre-operational phase of the CMEMS, and is also used at the Institute of Marine Research, Norway, for physical oceanography purposes as well as coupled ecosystem models. These three models represent the three main classes of numerical ocean models, namely z-level models, sigma-coordinate models and isopycnic-coordinate models. Moreover, the

inclusion of the ROMS model represents a high-resolution regional simulation specifically set up for studying the AW flow through the Nordic and Barents seas. This allows for a direct comparison between two large-domain models using data assimilation and a non-assimilating model dedicated to a specific region.

The aim of this paper is to objectively assess the performance (against observations) and agreement (between one another) of these models based on key metrics, such as ocean transports and temperature and salinity distribution and variability. We characterize the abilities of the models, with and without data assimilation, to reproduce the observed currents and water mass distribution as inferred from repeatedly sampled fixed sections. This includes an evaluation of the effect of using data assimilation in data-sparse high latitude seas. In addition, we point to some causes for differences between the models and observations, as well as among the models and model setups. Where possible, we relate the model-observational differences to model forcing or physics, based on oceanographic interpretation. In the end, we give some recommendations on ocean modelling in the Nordic Seas.

## 2. Data and methods

### 2.1. Ocean general circulation models

The NEMO model system is a z-level ocean model and it is documented in Lellouche et al., 2013, Ferry et al., 2012, and Madec et al., 2008. The following analysis includes results from a global simulation in both assimilation mode (NEMO-A) and free mode (NEMO-F). The current simulations use the LIM2 thermodynamic-dynamic sea ice model with an elastic-viscous-plastic rheology formulation. The NEMO-A uses a multi-data and multivariate reduced order Kalman filter based on the singular extended evolutive Kalman filter formulation. A bias correction scheme is included for temperature and salinity. The assimilated observations are delayed-time along-track satellite Sea Level Anomaly (SLA) from the Sea Level Thematic Assembly Center (TAC; http://marine.copernicus.eu), 25 km resolution Sea–Ice Concentration (SIC) from IFREMER/CERSAT, ¼° L4 Sea Surface Temperature (SST) from AVHRR sensor (Reynolds et al. 2007), and in-situ profiles of temperature and salinity (ARGO profiles principally) from the CORA3.3 database made available by the In Situ TAC (http://marine.copernicus.eu). In terms of data amount, no specific numbering is available for the Nordic seas as a whole in the system. However, a Barents Sea area is for example specifically monitored in which 2000 of satellite data (mainly from Envisat and Geosat) are assimilated on average in the system with a strong seasonal cycle. For the in situ data give similar statistics can give an erroneous view of the impact as the network has strongly evolved since the early 90's. However, and to give an idea, a maximum of few dozens of profiles per year are assimilated in the Barents Sea sector and so only during the end of the period. The in situ profiles are also better sampled in the 15–700 m depth layer. These data are assimilated on a weekly basis (7 days cycle) with an Incremental Analysis Update. Spatial (zonal and meridional directions) and temporal correlation scales are used to define an "influence bubble" around the analysis point in which data are also selected. In the Nordic seas these scales are about 150 km and 12 days.

The TOPAZ model system utilizes the hybrid-coordinate HYCOM model (Bleck, 2002) and has been documented in Sakov et al., 2012. The following analysis includes results from regional simulation covering the North Atlantic and Arctic in both assimilation mode (TOPAZ-A) and a free mode (TOPAZ-F). The simulations use a thermodynamic-dynamic sea ice model with an elastic-viscous-plastic rheology formulation from Hunke and Dukowicz (1997). TOPAZ-A uses the deterministic version of the ensemble Kalman Filter (Sakov and Oke, 2008) to assimilate remotely sensed SLA, SST, SIC, Lagrangian sea ice velocities (winter only, since 2002), and temperature and salinity profiles from Argo floats and research cruises. The data assimilation is performed weekly with a 100-members dynamical ensemble and an effective localization radius of 90 km. For more details on the assimilation procedure, including an analysis of the dynamical and multivariate effects of assimilation, see Sakov et al., 2012. TOPAZ does not include tides.

The ROMS model is a sigma-coordinate ocean model and is documented in Shchepetkin and McWilliams, 2005. The hindcast included in the following analysis is a regional simulation covering the Nordic, Barents and Kara seas, as well as the Nansen Basin in the Arctic Ocean. The model set-up and evaluation is documented in Lien et al., 2013a, 2014. The simulation uses a dynamic-thermodynamic sea ice module (Mellor and Kantha, 1989; Häkkinen and Mellor, 1992) based on an elastic-viscous-plastic rheology from Hunke and Dukowicz (1997), with two ice layers and a single snow layer. For more information on the sea-ice module, see Budgell (2005).

For further details on the ocean models the reader is referred to Table 1 and the references provided above.

### 2.2. Observations

We compare observations of hydrography and volume and heat transports from 5 repeatedly sampled fixed sections crossing the main gateways between the Nordic Seas and adjacent areas and also intercepting the AW flowing northward along the Norwegian continental slope. The sections are shown in Fig. 1. Positions, references and main characteristics are summarized in Table 2. Observations represent in-situ temperature, $T$, whereas modelled temperature represents potential temperature, $\Theta$. This study is mainly concerned with the upper 500 m of the water column, where the difference between the $T$ and $\Theta$ is less than 0.05 °C. For simplicity, we will therefore refer to both modelled and observed temperature as $T$.

#### 2.2.1. North Atlantic–Nordic Seas exchanges

Leaving out the negligible northward flow through the English Channel to the North Sea (0.1 Sv; 1 Sv = $10^6$ $m^3/s$) and the northward flow of AW through the Denmark Strait between Iceland and Greenland (<1 Sv; Jónsson and Valdimarsson, 2012), the northward flow of AW from the North Atlantic to the Nordic Seas occur through the two openings: The Færøy–Shetland Channel (FSC) and the Iceland–Færøy Ridge (Hansen and Østerhus, 2000).

Monthly averages of net AW ($T > 5$ °C, $S > 35.0$) volume transport through the FSC are obtained from Berx et al., 2013. The salinity maximum and the corresponding temperature at the Shetland slope are measured irregularly and used to define the core of the AW inflow through the FSC. Similarly, we extract the modelled salinity maximum and corresponding temperature within the FSC.

The Iceland–Færøy branch is monitored on the northern Færøy slope, hereinafter termed Færøy North (FN; Østerhus et al., 2005). The modelled net AW volume and heat transports are calculated using the same AW definition as for the FSC.

#### 2.2.2. Svinøy Northwest section

The Svinøy Northwest (SNW) section intercepts the two-branched Norwegian Atlantic Current flowing northward along the Norwegian continental slope. Here, we focus on the well-documented and continuously monitored eastern branch, commonly termed the Norwegian Atlantic slope Current (e. g., Orvik and Skagseth, 2005; see Table 2). The observation-based volume and heat transport estimates are based on a single current meter record, which has been found to represent 74% of the variability of the total AW volume transport on monthly time scales (Orvik and Skagseth 2003). The hourly observations are filtered by a 30-day

**Table 1**
Summary of the model simulations.

| Model | TOPAZ-F | TOPAZ-A | NEMO-F | NEMO-A | ROMS |
|---|---|---|---|---|---|
| Area | North Atlantic + Arctic | North Atlantic + Arctic | Global | Global | Nordic Seas |
| Open boundary forcing | WOA T/S climatology | WOA T/S climatology | – | – | Simple Ocean Data Assimilation (SODA) 2.1.6. Global reanalysis |
| Horizontal res | 11–16 km | 11–16 km | ¼ degree | ¼ degree | 4 km |
| Vertical res | 28 layers | 28 layers | 50 layers | 75 layers | 32 layers |
| Vertical coordinate | z-isopycnal | z-isopycnal | z | z | Sigma |
| Atmospheric forcing | ERA Interim (Dee et al., 2011) | ERA Interim (Dee et al., 2011) | ERA Interim (Dee et al., 2011) | ERA Interim (Dee et al., 2011) | Norwegian reanalysis (NORA) 10 km (Reistad et al., 2011) |
| Tidal forcing | None | None | None | None | Eight constituents from global ocean tides model (TPXO4) |
| Assimilated data | – | SLA, SST, sea–ice concentration and velocity, T+S profiles from Argo buoys and research cruises | – | SLA, SST, sea–ice concentration, T+S profiles from the CMEMS In Situ Thematic Assembly Center | Surface relaxation of salinity (180 days) |
| Assimilation method | – | Deterministic ensemble Kalman filter | – | Singular extended evolutive Kalman filter | – |

moving average and re-sampled at the 15th of each calendar month. The modelled volume and heat transports are calculated using the common AW definition in the SNW ($T > 5$ °C; $S > 35$; Orvik et al., 2001) and the full section inshore of the 1000 m isobath.

### 2.2.3. Barents Sea Opening

For the western entrance to the Barents Sea, commonly termed the Barents Sea Opening (BSO), we use time series of temperature and salinity averaged between 50 and 200 m depth and between 71°N30' and 73°N30' obtained from the Norwegian Marine Data Center http://www.imr.no/sjomil/index.html (Blindheim and Loeng 1981). The modelled estimates were computed similarly by linearly interpolating monthly averages to the observation dates.

Observation-based estimates of volume and heat transports through the BSO are calculated using a box-model approach on an array of current meter moorings extending from 71°30′N to 73°30′N (Ingvaldsen et al., 2002). Due to occasions of relatively large sampling errors and drift in some of the conductivity cells attached to the current meters, the AW is defined by $T > 3$ °C only. The AW is distinguishable from the Polar Water in the northern BSO through its considerably higher temperature. The Norwegian coastal current, which flows through the BSO to the south, has a temperature comparable to the AW, but it is considerably less saline. However, the front between the AW and the coastal current is only occasionally located north of 71°30′N. Hence, using only temperature within the chosen geographical boundary to separate the AW from the coastal water is considered to be adequate. The observations are sampled at 20 min intervals and filtered using a fourth-order Butterworth filter and then re-sampled at the 15th day of each month. Modelled volume and heat transports are calculated from monthly mean velocity and temperature in the mooring array part of the section (71°30′N to 73°30′N), by applying a similar water mass definition.

### 2.2.4. Fram Strait

In the Fram Strait between Greenland and the Svalbard archipelago we base our comparison on the results reported by Beszczynska-Möller et al. (2012) for the West Spitsbergen Current, which carries AW through the eastern part of the section along the Spitsbergen shelf.

## 2.3. Statistical methods

Our analysis includes comparison of correlation coefficients, mean values, standard deviations, trends and seasonal cycles. All time series have their average monthly seasonal cycle and linear trend removed prior to the correlation analysis. The significance of the correlations are tested using the inverse Student's T cumulative distribution function with $N-1$ degrees of freedom, where $N$ is the number of observations. A minimum confidence level of 95% is chosen for all correlation coefficients.

For a straightforward comparison with observations-based heat transport estimates, the modelled heat transports are calculated using cross-section velocity and temperature relative to the widely adopted reference temperature $T_{ref} = -0.1$ °C (Aagaard and Greisman, 1975).

For the BSO and the FSC we perform a two-step comparison of ocean transports. In the first step, we use the common reference level for defining AW and in the BSO we use only the part of the section covered by the mooring array. This is a rather strict comparison which will uncover possible features such as misplacement of currents due to the differences in model and real-world bathymetry, among other things. In the second step, we inspect the model results with the aim to uncover discrepancies that affect the result of the comparison, such as temperature or salinity

**Table 2**
Section names, positions and Atlantic Water definitions. *Salinity criterion is only used in modelled full section.

| Section name | Section position | Atlantic Water |
|---|---|---|
| Færøy North (FN) | 62°25′ N, 6°W to 65°30′ N, 6°W | $T > 5$ °C; $S > 35.0$ |
| Færøy–Shetland Channel (FSC) | 61°20'N, 6°30'W to 59°30'N 3°W | $T > 5$ °C; $S > 35.0$ |
| Svinøy Northwest (SNW) | 62°30'N,5°E to 63°10'N, 3°40'E | $T > 5$ °C; $S > 35.0$ |
| Barents Sea Opening (BSO) | 70°15'N, 20°E to 74°15'N, 19°30'E | $T > 3$ °C; ($S > 35.0$)* |
| Fram strait (FS) | 78°50'N, 8°W to 78°50'N, 10°E | $T > 2$ °C |

**Table 3**
Criteria for determining model score on various statistical parameters. Note the two-sided criteria for standard deviation and trend (i.e., the model can be higher or lower than the observations). The score ranges from 0 points (worst) to 3 points (best).

| Parameter/points | 0 | 1 | 2 | 3 |
|---|---|---|---|---|
| Mean (abs(model-obs))/obs std | > 1 | [1–0.5 > | [0.5–0.25 > | ≤ 0.25 |
| Standard deviation (model/obs) | > 3<br>< 1/3 | [3–2 ><br>[1/3–1/2 > | [2–1.5 ><br>[1/2–2/3 > | ≤ 1.5<br>≥ 2/3 |
| Trend (model/obs) | Wrong sign<br>>3<br><1/3 | [3–2 ><br>[1/3–1/2 > | [2–1.5 ><br>[1/2–2/3 > | ≤ 1.5<br>≥ 2/3 |
| Correlation (95% confidence = X) | < X | ≥ X<br>< X + (1-X)/2 | ≥ X + (1-X)/2<br>< X + 3(1-X)/4 | ≥ X + 3(1-X)/4<br>≤ 1 |

**Table 4**
Statistics of parameters in the Barents Sea Opening. Colour codes are based on criteria shown in Table 3 (green = 3 points, yellow = 2 points, red = 1 point, black = 0 points). Correlations significant to the 99% level are shown in boldface and correlations significant to the 95% level are shown in italics. Non-significant correlations are shown as n.s. Bottom row shows overall score for each model calculated with equal weight to each parameter and the colours represent the nearest integer. (For interpretation of the references to colour in this table legend, the reader is referred to the web version of this article.)

| Parameter | Obs | TOPAZ-F | TOPAZ-A | NEMO-F | NEMO-A | ROMS |
|---|---|---|---|---|---|---|
| V seas corr | – | *0.58* | *0.64* | *0.67* | **0.72** | *0.67* |
| V mean (Sv) | 2.0 | 1.2 | 1.7 | 2.2 | 1.8 | 2.3 |
| V std (Sv) | 1.0 | 0.4 | 0.6 | 0.7 | 0.7 | 1.0 |
| V trend (Sv/year) | 0.023 | – 0.023 | 0.000 | – 0.050 | – 0.013 | 0.037 |
| V corr | – | **0.29** | **0.27** | **0.32** | **0.36** | **0.36** |
| Q seas corr | – | *0.69* | **0.76** | **0.80** | **0.83** | **0.76** |
| Q mean (TW) | 50 | 23 | 37 | 55 | 42 | 52 |
| Q std (TW) | 22 | 7 | 13 | 14 | 16 | 25 |
| Q trend (TW/year) | 0.68 | –0.23 | 0.31 | – 0.74 | – 0.01 | 1.55 |
| Q corr | – | **0.35** | **0.33** | **0.32** | **0.42** | **0.40** |
| T seas corr | – | **0.98** | *0.91* | **0.95** | **0.92** | **0.94** |
| T mean (°C) | 5.69 | 4.59 | 5.30 | 5.26 | 5.33 | 5.11 |
| T std (°C) | 0.62 | 0.47 | 0.51 | 0.66 | 0.64 | 0.85 |
| T trend (°C/year) | 0.065 | 0.062 | 0.053 | 0.078 | 0.062 | 0.070 |
| T corr | – | **0.70** | **0.69** | **0.36** | **0.62** | **0.54** |
| S seas corr | – | *0.83* | n.s. | *0.85* | n.s. | n.s. |
| S mean | 35.08 | 35.05 | 35.02 | 34.96 | 35.10 | 34.97 |
| S std | 0.04 | 0.02 | 0.03 | 0.08 | 0.06 | 0.06 |
| S trend (1/year) | 0.0060 | 0.0011 | 0.0008 | 0.0029 | 0.0095 | 0.0073 |
| S corr | – | n.s. | **0.55** | **-0.36** | **0.29** | **0.68** |
| BSO AVG | – | **1.05** | **1.35** | **1.50** | **1.75** | **1.80** |

biases or displacement of main current branches, and re-calculate the volume and heat transports using bias-adjusted temperature and salinity criteria applied on the full sections.

In order to assess the model performance regarding the parameters we have chosen to include in our investigation and within the geographic sections studied, we have calculated a score for each model in each section. The score ranges from 0 points (worst) to 3 points (best), and are based on the criteria listed in Table 3 (model-data mean value difference, model/data standard deviation ratio, trend and correlation), for each of the parameters temperature ($T$), salinity ($S$), volume ($V$) and heat ($Q$) transports. The colour coded results are presented in Tables 4–9 and summarized in Table 10. However, the assessment has some caveats, amongst them that the score is sensitive to our choice of objective criteria for each statistical parameter. Therefore, the score should be

**Table 5**
Same as Table 4, but using the full BSO section for the model results and water mass definitions adjusted according model bias.

| Parameter | Obs | TOPAZ-F | TOPAZ-A | NEMO-F | NEMO-A | ROMS |
|---|---|---|---|---|---|---|
| V seas corr | | n.s. | n.s. | *0.68* | *0.66* | **0.72** |
| V mean (Sv) | 2.0 | 1.3 | 1.6 | 3.2 | 2.8 | 2.1 |
| V std (Sv) | 1.0 | 0.3 | 0.5 | 0.9 | 0.9 | 1.1 |
| V trend (Sv/year) | 0.023 | -0.000 | 0.028 | –0.024 | 0.010 | 0.045 |
| V corr | – | **0.23** | **0.26** | **0.30** | **0.39** | **0.43** |
| Q seas corr | | n.s. | n.s. | **0.75** | **0.75** | **0.76** |
| Q mean (TW) | 49 | 24 | 33 | 81 | 67 | 49 |
| Q std (TW) | 22 | 6 | 11 | 23 | 22 | 27 |
| Q trend (TW/year) | 0.68 | 0.26 | 0.92 | –0.29 | 0.54 | 2.35 |
| Q corr | – | **0.29** | **0.30** | **0.35** | **0.45** | **0.43** |

**Table 6**
Same as Table 4 but for the Færøy–Shetland Channel. (For interpretation of the references to colour in this table legend, the reader is referred to the web version of this article.)

| Parameter | Obs | TOPAZ-F | TOPAZ-A | NEMO-F | NEMO-A | ROMS |
|---|---|---|---|---|---|---|
| V seas corr | – | **0.82** | **0.87** | **0.83** | **0.89** | *0.64* |
| V mean (Sv) | 2.7 | 1.7 | 1.8 | 1.7 | 1.7 | 2.4 |
| V std (Sv) | 1.0 | 0.3 | 0.5 | 0.8 | 1.0 | 2.2 |
| V trend (Sv/year) | 0.002 | 0.015 | 0.017 | –0.042 | 0.035 | –0.007 |
| V corr | – | **0.36** | **0.54** | **0.33** | **0.41** | **0.28** |
| Q mean (TW) | 107 | 57 | 63 | 79 | 68 | 90 |
| T seas corr | – | **0.83** | **0.90** | **0.84** | **0.90** | *0.68* |
| T mean (°C) | 10.03 | 10.57 | 10.12 | 9.71 | 9.39 | 8.73 |
| T std (°C) | 0.60 | 2.09 | 1.64 | 1.71 | 1.32 | 2.79 |
| T trend (°C/year) | 0.039 | 0.052 | 0.063 | 0.046 | 0.059 | 0.061 |
| T corr | – | **0.37** | **0.46** | **0.27** | **0.37** | n.s. |
| S seas corr | – | n.s. | **0.88** | n.s. | **0.78** | n.s. |
| S mean | 35.40 | 35.37 | 35.32 | 35.41 | 35.37 | 35.27 |
| S std | 0.04 | 0.02 | 0.03 | 0.02 | 0.06 | 0.06 |
| S trend (1/year) | 0.0046 | –0.0033 | 0.0037 | –0.0005 | 0.0061 | 0.0157 |
| S corr | – | n.s. | **0.32** | *0.24* | **0.30** | n.s. |
| **FSC AVG** | – | **0.87** | **1.60** | **1.33** | **1.47** | **0.67** |

**Table 7**
Same as Table 6, but with water mass definitions adjusted according model bias.

| Parameter | Obs | TOPAZ-F | TOPAZ-A | NEMO-F | NEMO-A | ROMS |
|---|---|---|---|---|---|---|
| V seas corr | | **0.82** | **0.87** | **0.82** | **0.88** | n.s. |
| V mean (Sv) | 2.7 | 1.7 | 1.9 | 1.7 | 1.6 | 2.0 |
| V std (Sv) | 1.0 | 0.3 | 0.5 | 0.8 | 1.1 | 2.6 |
| V trend (Sv/year) | 0.002 | 0.015 | 0.015 | –0.042 | 0.036 | 0.003 |
| V corr | – | **0.36** | **0.56** | **0.32** | **0.41** | **0.28** |
| Q mean (TW) | 107 | 59 | 64 | 77 | 66 | 84 |

**Table 8**
Same as Table 4 but for the Færøy North section. (For interpretation of the references to colour in this table legend, the reader is referred to the web version of this article.)

| Parameter | Obs | TOPAZ-F | TOPAZ-A | NEMO-F | NEMO-A | ROMS |
|---|---|---|---|---|---|---|
| V seas corr | – | n.s. | n.s. | n.s. | n.s. | n.s. |
| V mean (Sv) | 3.5 | 1.9 | 1.5 | 3.0 | 2.3 | 1.8 |
| V std (Sv) | 0.8 | 0.5 | 0.8 | 0.5 | 0.7 | 0.8 |
| V trend (Sv/year) | – 0.007 | 0.013 | 0.015 | – 0.029 | 0.023 | 0.102 |
| V corr | – | n.s. | n.s. | n.s. | **0.36** | *0.19* |
| Q (TW) | 134 | 55 | 46 | 87 | 67 | 48 |
| **FN AVG** | – | **0.40** | **0.60** | **0.60** | **0.80** | **0.80** |

**Table 9**
Same as Table 4 but for the Svinøy Northwest section. (For interpretation of the references to colour in this table legend, the reader is referred to the web version of this article.)

| Parameter | Obs | TOPAZ-F | TOPAZ-A | NEMO-F | NEMO-A | ROMS |
|---|---|---|---|---|---|---|
| V seas corr | – | **0.82** | **0.75** | n.s. | n.s. | n.s. |
| V mean (Sv) | 4.4 | 0.6 | 1.4 | 2.2 | 2.3 | 2.8 |
| V std (Sv) | 1.0 | 0.6 | 0.8 | 0.6 | 0.7 | 2.0 |
| V trend (Sv/year) | 0.027 | 0.000 | 0.025 | –0.037 | 0.056 | 0.121 |
| V corr | – | **0.20** | **0.55** | **0.38** | **0.54** | **0.33** |
| Q seas corr | – | **0.85** | **0.77** | 0.62 | n.s. | *0.61* |
| Q mean (TW) | 161 | 18 | 42 | 73 | 74 | 86 |
| Q std (TW) | 34 | 16 | 25 | 21 | 23 | 62 |
| Q trend (TW/year) | 1.8 | 0.1 | 0.9 | –1.0 | 2.2 | 4.4 |
| Q corr | – | 0.18 | **0.53** | **0.36** | **0.54** | **0.36** |
| **SNW AVG** | – | **0.90** | **1.50** | **0.70** | **1.10** | **0.70** |

**Table 10**
Summary of the overall score for each model separated in sections and parameters, based on Tables 3, 5, 7, 8. The section and parameter averages are calculated with equal weight to each section and parameter, respectively. The colours represent the nearest integer (green = 3 points, yellow = 2 points, red = 1 point, black = 0 points). (For interpretation of the references to colour in this table legend, the reader is referred to the web version of this article.)

| Section/model | TOPAZ-F | TOPAZ-A | NEMO-F | NEMO-A | ROMS |
|---|---|---|---|---|---|
| BSO AVG | 1.05 | 1.35 | 1.50 | 1.75 | 1.80 |
| FSC AVG | 0.87 | 1.60 | 1.33 | 1.47 | 0.67 |
| FN AVG | 0.40 | 0.60 | 0.60 | 0.80 | 0.80 |
| SNW AVG | 0.90 | 1.50 | 0.70 | 1.10 | 0.70 |
| **SEC AVG** | **0.81** | **1.26** | **1.03** | **1.28** | **0.99** |
| T AVG | 1.80 | 2.10 | 1.80 | 1.80 | 1.30 |
| S AVG | 0.60 | 1.30 | 0.90 | 1.60 | 0.90 |
| V AVG | 0.75 | 1.10 | 1.05 | 1.15 | 1.00 |
| Q AVG | 0.60 | 1.30 | 1.20 | 1.50 | 1.40 |
| **PAR AVG** | **0.94** | **1.45** | **1.24** | **1.51** | **1.15** |
| **TOT AVG** | **0.90** | **1.34** | **1.20** | **1.44** | **1.14** |

viewed as a performance guide and not a final standing of the different models. Moreover, the temperature and salinity measurements used in our analysis are also assimilated into the re-analysis simulations. Thus, there are inherent dependencies between the observed and modelled hydrography in the simulations with assimilation, whereas the modelled and observed volume and heat transports are independent.

## 3. Results

For all 5 sections we have compared the 5 model simulations with the observations. We do show the analysis from one well covered section, the BSO, in full, while for the remaining sections the results are summarized in tables and presented as figures in the Supplementary material section.

### 3.1. Barents Sea Opening

#### 3.1.1. Volume and heat transports

The most fundamental source of variability is the seasonal cycle. Inability to capture the seasonal cycle therefore indicates that the model contain fundamental errors. All the model simulations reproduce the observed seasonal patterns through the BSO at 95% confidence for the volume transports and 99% (except for TOPAZ-F) for the heat transports (Fig. 2; Table 4). Moreover, the volume and heat transport seasonal amplitudes in TOPAZ-A and both NEMO simulations are comparable to the observations, whereas the TOPAZ-F seasonal amplitude is smaller and the ROMS seasonal amplitude is larger than observed.

The long-term average (1997–2009) observation-based estimate of net AW volume transport through the BSO is 2.0 Sv, with a standard deviation of 1.0 Sv. The corresponding modelled volume transports are shown in Fig. 3 and summarized in Table 4. The lowest volume transport (1.2 Sv) is found in the TOPAZ-F, increasing to 1.7 Sv in the TOPAZ-A. The volume transport in NEMO-F is slightly on the high side (2.2 Sv) and in NEMO-A slightly lower than the observations (1.8 Sv). The variability is less in both TOPAZ and NEMO, compared with the observations. ROMS has the highest modelled volume transport (2.3 Sv), as well as the highest standard deviation (1.0 Sv). The observations show a positive trend of 0.023 Sv/year. TOPAZ-F (−0.023 Sv) and both NEMO-F and NEMO-A (−0.050 Sv and −0.013 Sv, respectively) have negative trends, while ROMS has a positive trend of 0.036 Sv/year and TOPAZ-A has no trend in the volume transport

Looking at the remaining variability, i.e., with the seasonal cycle and long-term trend removed, we find that the correlations between modelled and observed volume transports are generally low, although significant at 99% confidence for all simulations (Table 4).

The heat transports resemble the volume transports (Supplementary Fig. S1; Table 4). Both TOPAZ simulations are on the low side, especially the free simulation, while NEMO-F and NEMO-A have larger and smaller heat transports, respectively, compared with the observations. ROMS shows the closest agreement with the observed heat transports, both in terms of average and standard deviation. The correlations between observed and modelled heat transports are comparable to those for volume transports, i.e., generally low but significant. Among the outstanding features in the volume and heat transport time series are two distinct peaks in all model simulations in the winters of 1999/00 and 2004/05, that are not seen in the observations. On the contrary, the two most outstanding episodes recorded in the observations, an exceptional high in 2006 and an exceptional low in 2007, are only to some degree seen as anomalies in the model simulations.

#### 3.1.2. Hydrography and current structure

To compare the hydrographic properties of the AW entering the Barents Sea through the BSO, we derive the statistical properties of the integrated temperature and salinity time series as described above. The time series from all the model simulations are significantly correlated with the observations in terms of seasonal temperature variations, while only the free simulations, including ROMS, are significantly correlated with observations in terms of seasonal salinity variations. All the simulations have a cold bias in terms of long-term average of temperature (Table 4), with the largest bias in TOPAZ-F (−1.10 °C). This temperature bias is reduced to −0.39 °C in TOPAZ-A, which is comparable to both simulations using NEMO (Table 4; Fig. 4). All the simulations, except NEMO-A, have a fresh bias (Table 4; Fig. 5), with the largest biases found in ROMS (-0.11) and NEMO-F (−0.12). Looking at trend throughout the investigation period, all the simulations have temperature trends which are comparable to the observed trend. For salinity, NEMO-A and ROMS have stronger trends than the observed trend, while the trend in NEMO-F and both simulations using TOPAZ are weaker than observed (Table 4).

The temperature variability (with average seasonal variation and linear trend removed) is significantly correlated with observed variability in all the simulations, with the highest correlations

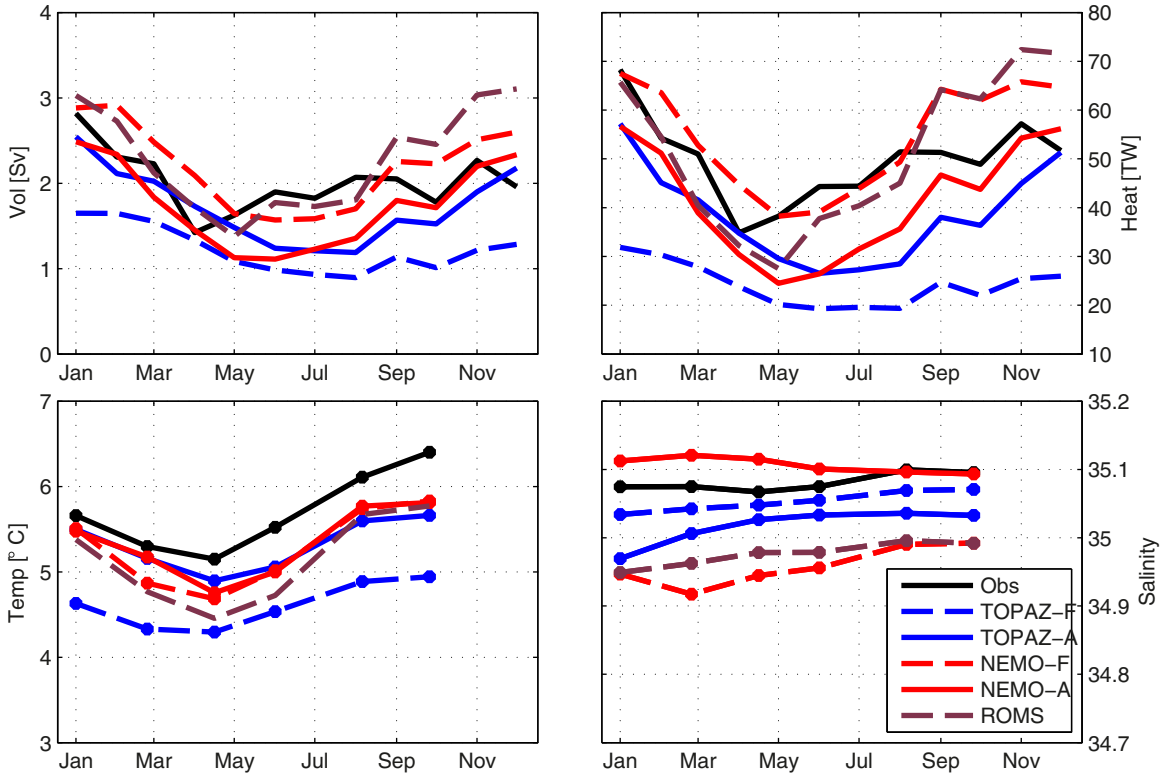


**Fig. 2.** Seasonal cycle in Barents Sea Opening net Atlantic Water ($T > 3$ °C) volume transport (top left), net Atlantic Water heat transport (relative to $T = -0.1$ °C; top right), temperature between 50 and 200 m depth (bottom left), salinity between 50 and 200 m depth (bottom right) between 71°30'N and 73°30'N. Note that for temperature and salinity, observations only exist six times each year (indicated by dots). Therefore, the model values (monthly averages) are linearly interpolated to the date of observations. Volume and heat transport averages represent the period 1997–2009. Temperature and salinity averages represent the period 1993–2009.

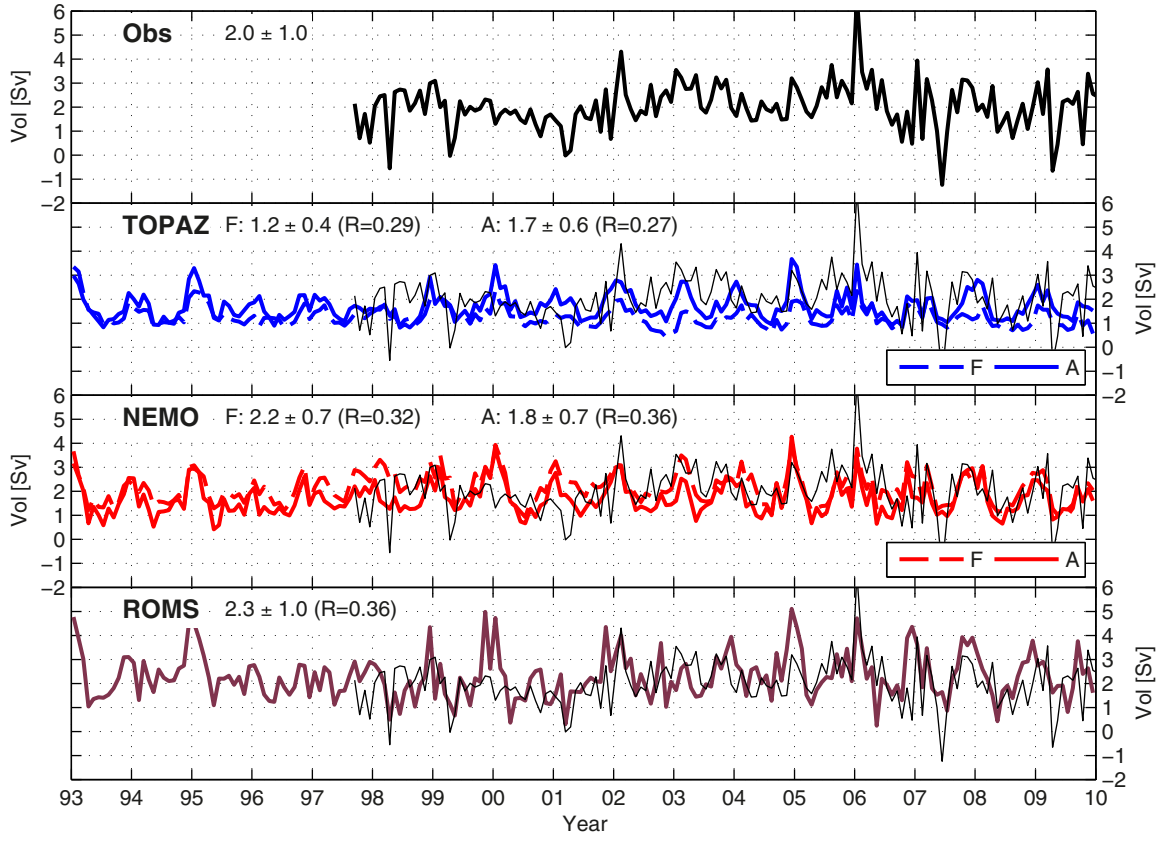


**Fig. 3.** Monthly net Atlantic Water ($T > 3$ °C) volume transport through the Barents Sea Opening between 71°30'N and 73°30'N. The observations are plotted in all panels for direct comparison with the model results (thin, black lines). Average values, standard deviations and correlation with observations during the period covered by the observations are indicated. Positive values are toward the east. All values are in Sverdrups.

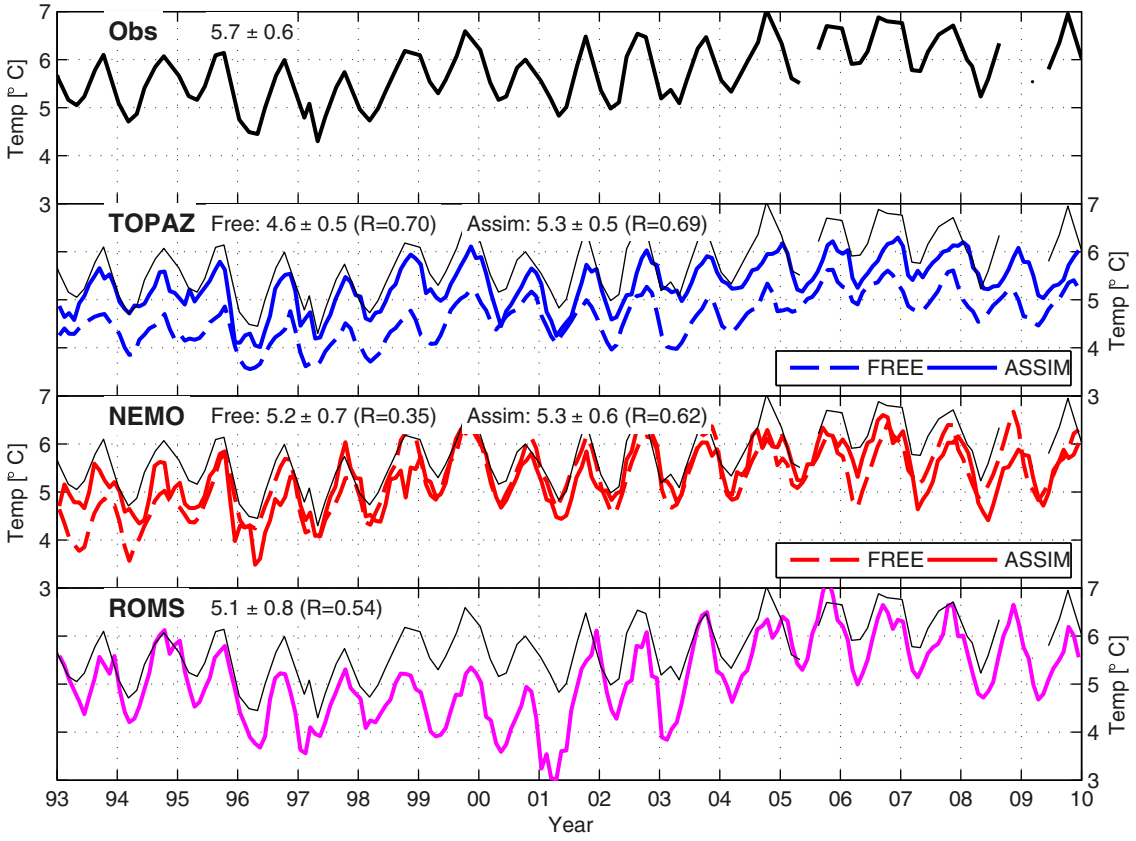


**Fig. 4.** Average temperature in the Barents Sea Opening between 71°30'N and 73°30'N and between 50 and 200 m depth. The observations are plotted in all panels for direct comparison with the model results (thin, black lines). Observations only exist six times each year, model values are monthly averages. Average values, standard deviations and correlation with observations during the period covered by the observations are indicated. All values are in degrees Celsius (°C).

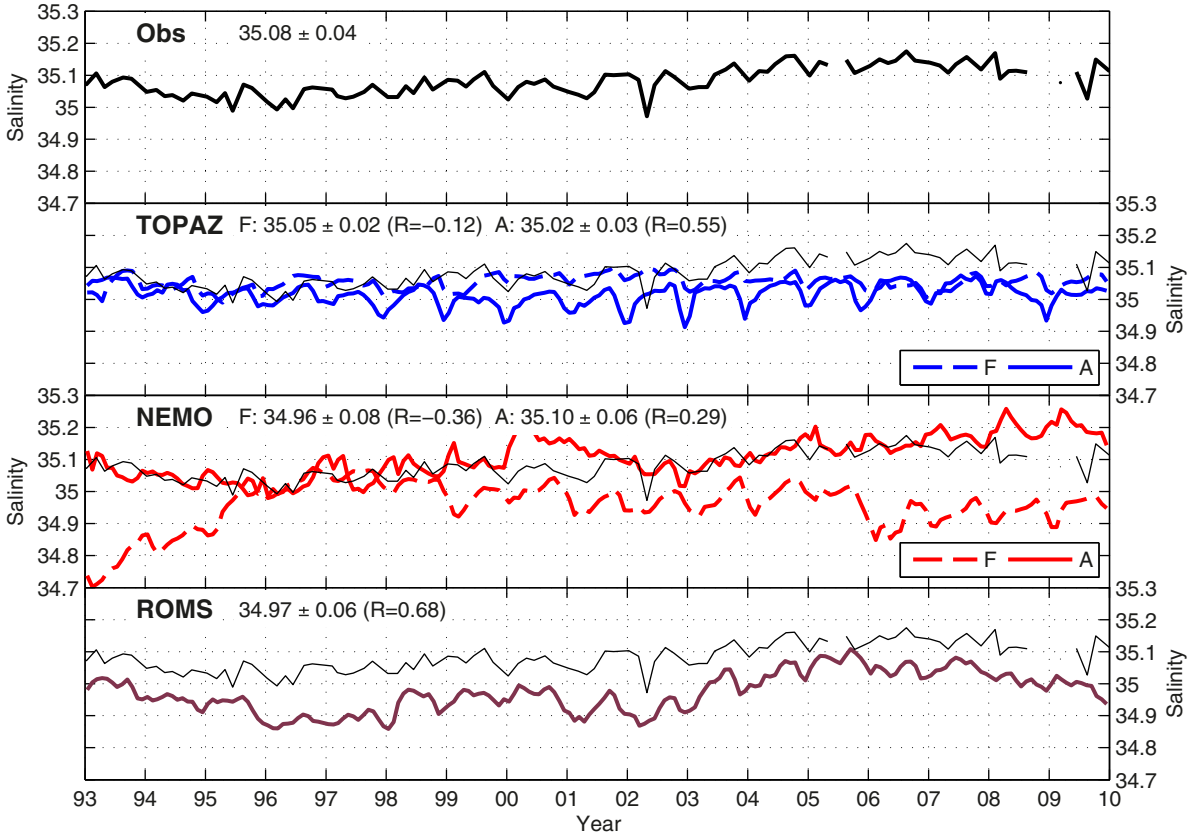


**Fig. 5.** Average salinity in the Barents Sea Opening between 71°30'N and 73°30'N and between 50 and 200 m depth. The observations are plotted in all panels for direct comparison with the model results (thin, black lines). Observations only exist six times each year, model values are monthly averages. Average values, standard deviations and correlation with observations during the period covered by the observations are indicated.

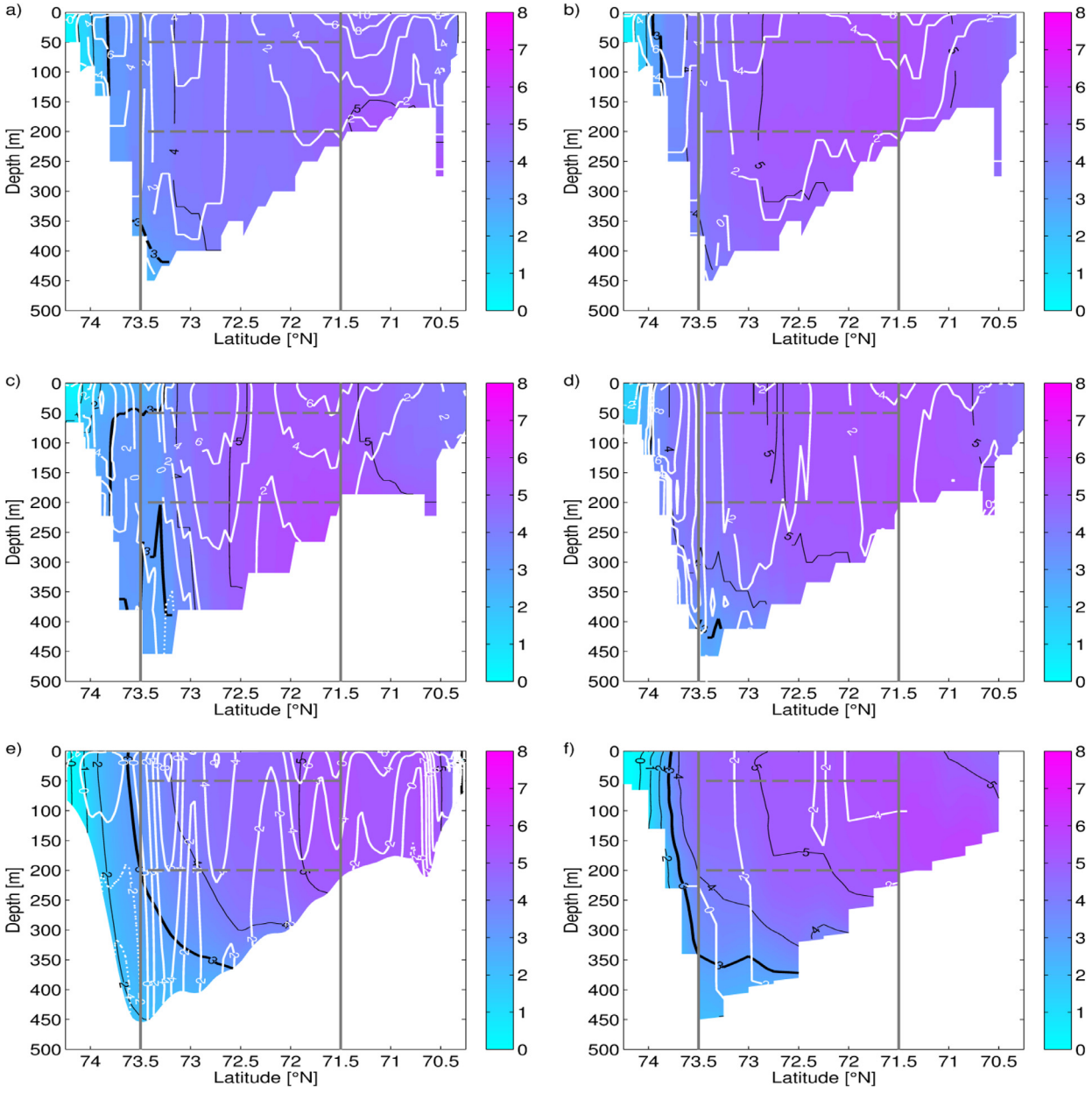


**Fig. 6.** Cross section through the Barents Sea Opening showing average temperature (colour; black isolines) and velocity normal to section (white isolines) in March. (a) TOPAZ Free; (b) TOPAZ Assimilated; (c) NEMO Free; (d) NEMO Assimilated; (e) ROMS; (f) observations. Temperature and modelled currents represent the period 1993–2009. Observed currents represent the period 1997–2009. Thick, black lines show the 3 °C isotherm, i.e., the extent of the Atlantic Water. Gray vertical lines show the part of the section covered by moored current meters in which volume and heat transports are calculated. Horizontal gray, broken lines show the box in which average temperature and salinity is calculated. Temperatures are in °C and velocities are in cm/s.

found in both the simulations using TOPAZ. In NEMO the correlation increases from $R = 0.36$ in the free simulation to $R = 0.62$ in the assimilated simulation. Looking at the variability in salinity, we find that all simulations, with the exception of TOPAZ-F, are significantly correlated with observed variability, but in NEMO-F the correlation is negative ($R = -0.36$). The highest correlation is found in ROMS ($R = 0.68$).

All the model simulations resemble the main hydrographic features observed within the BSO (Figs. 6 and 7). Coastal water in the southernmost part of the section is separated from the AW in the central part of the section by a wedge-shaped haline front located approximately over the 200 m isobath at 71°N. To the north, the Polar Front on the northern slope of the Bear Island Trough separates the AW from the colder and less saline Polar Water. In ROMS, the front between the AW and the coastal water is steeper and located further south than in the observations, whereas NEMO-F has excessive amounts of coastal water. Furthermore, ROMS has a large portion of Polar Water on the northern slope, whereas the higher temperatures in TOPAZ in this area suggest that the water masses have a substantial AW component. During summer, the coastal water extends further to the north along with an upper layer thermal stratification (Supplementary Figs. S2, S3). The wedge-shaped front between the coastal current and the AW during summer is well represented in the simulations with TOPAZ and NEMO, while the front is too steep in ROMS also in summer.

Mean profiles of temperature and salinity, as well as *T-S* diagrams, representing hydrographic properties in March (1993–2009 average) at 3 different positions (see map; Fig. 1) along the BSO section are shown in Figs. 8 and 9. Results representing September averages are shown in Supplementary Figs. S4, S5. On the

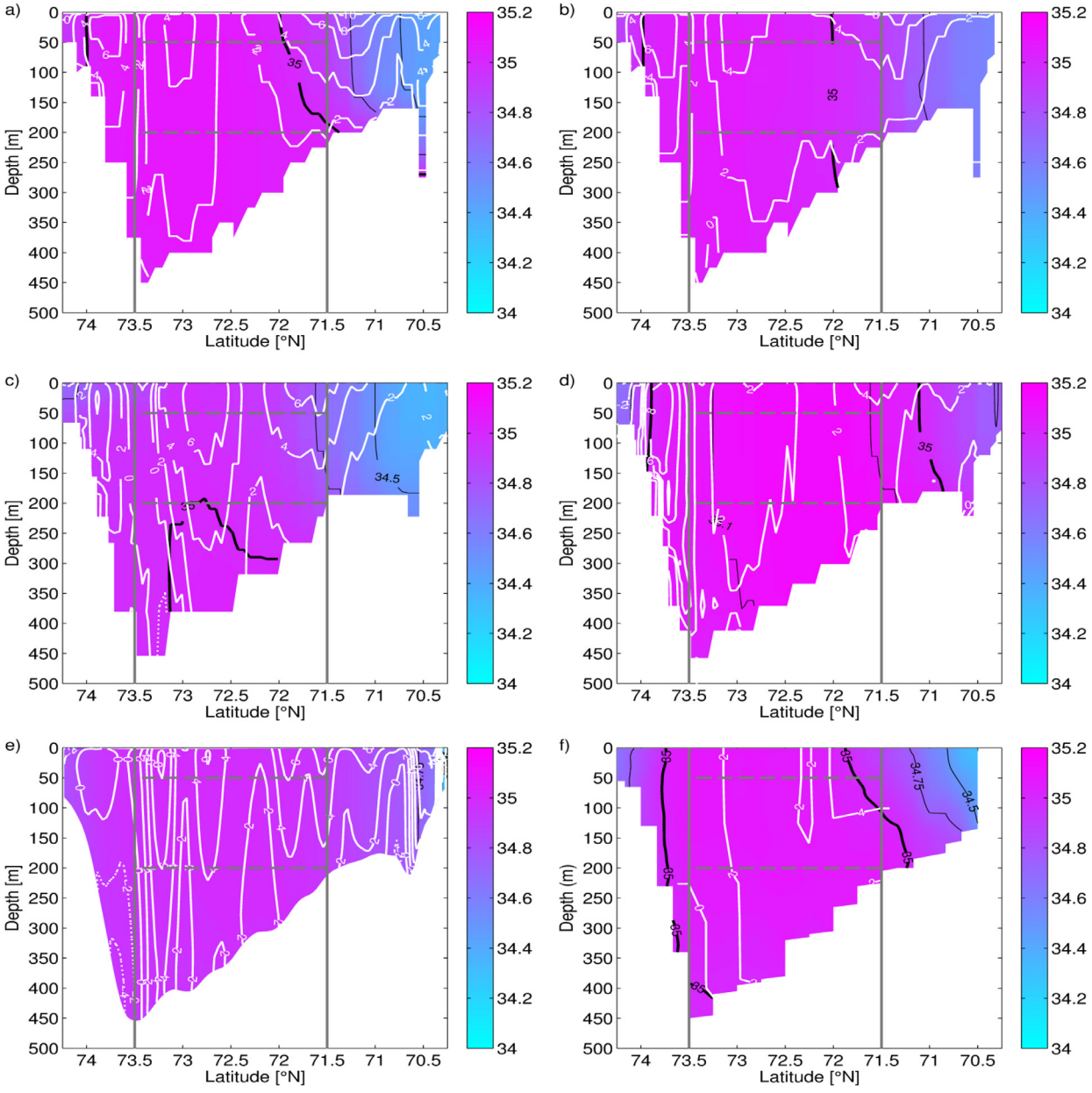


**Fig. 7.** Same as Fig. 6, but for salinity. Thick black line is the 35.0 isohaline.

southernmost location, all models have a cold bias during winter, but the assimilated simulations are closer to the observations compared with the free simulations. Also, all simulations, except the TOPAZ-F, are within the range of the observations. In terms of salinity, NEMO-F clearly has a larger presence of coastal water at 71°30'N compared with the observations, whereas the salinity in NEMO-A has a positive bias. The other three simulations have a negative bias, but they mostly remain within the observed range. However, the vertical stratification is less pronounced in all simulations compared with the observations. The *T-S* diagram shows how the differences in hydrographic properties are affecting the density distribution (Fig. 9). ROMS and TOPAZ-A have densities that are comparable to the observed values, albeit with less variability throughout the water column. NEMO-F has less dense water masses, while NEMO-A and TOPAZ-F have denser water masses than observed at 71°30'N. In summer, the stratification due to insolation and subsequent heating as well as increased amounts of freshwater from the coastal current is evident (Supplementary Fig. S4). NEMO-F resembles the observed temperature profile the most. The assimilation clearly increases both the thermocline and halocline depth in TOPAZ towards the observed values, although in both cases the stratification is reduced and becomes too weak compared with the observations. Interestingly, in NEMO, the salinity in NEMO-F is closer to the observations within the mixed-layer and upper halocline, whereas in NEMO-A the salinity is closer to the observations in the lower halocline and below. ROMS shows a fairly good agreement with the observed temperature structure, while the halocline is too weak and shallow.

In the central part of the BSO (72°30'N), all the simulations tend to have a cold bias, although they are all within the observed temperature range during winter (Fig. 8). The ROMS vertical temperature structure resembles the observations, whereas the other simulations have less vertical thermal stratification. In salinity NEMO-A has a saline bias, whereas the other simulations have fresh biases. Again, ROMS has the vertical structure that resembles the observations the most in terms of gradients but lies outside the observed range in terms of absolute values, whereas the other simulations have too weak vertical gradients. These differences also appear in

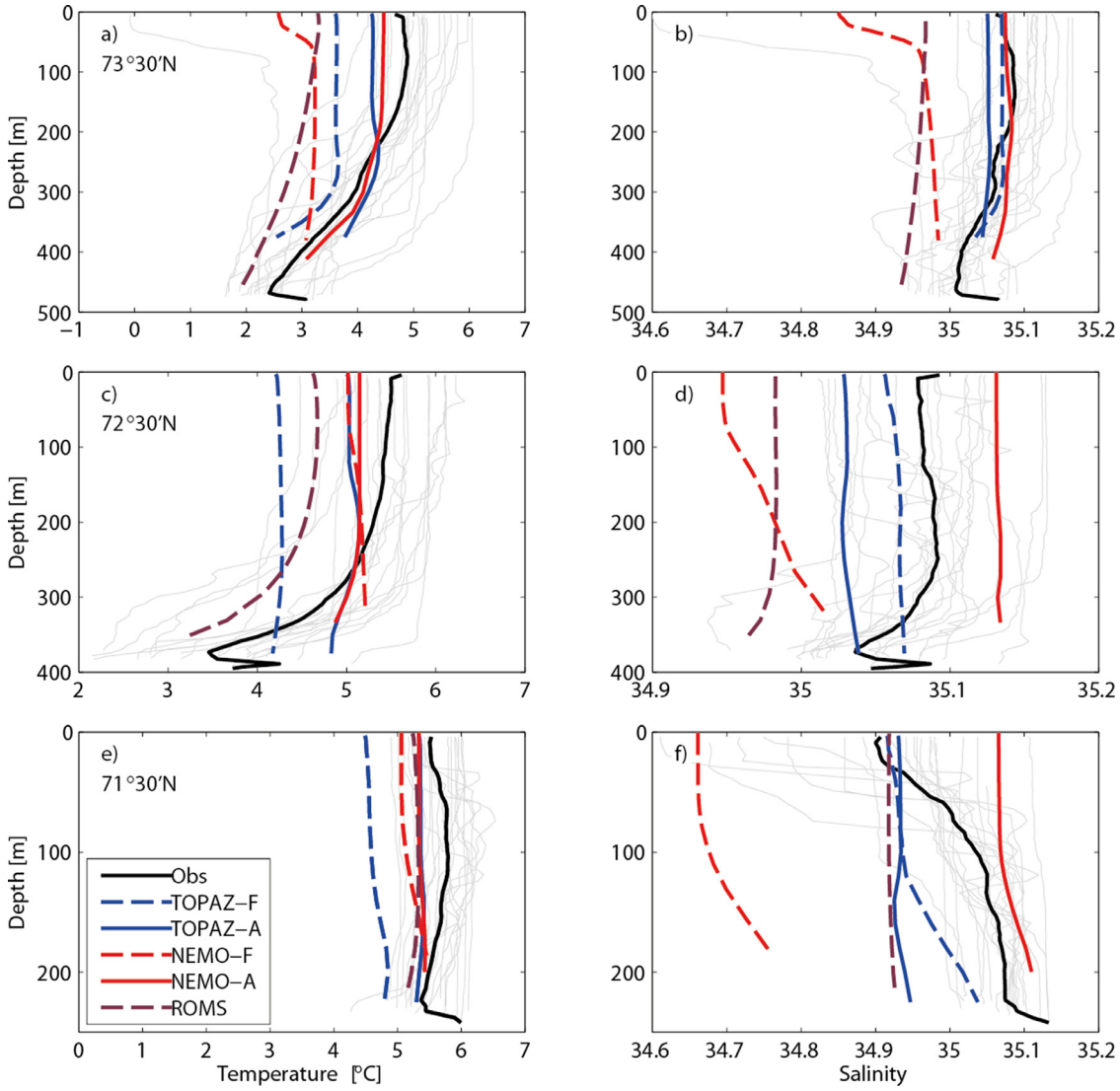


**Fig. 8.** Vertical profiles of *T* and *S* in the Barents Sea Opening averaged over the period March 1993–2009 (thick lines) and all observations obtained during the period (thin, gray lines). (a) temperature at 73°30′N; (b) salinity at 73°30′N; (c) temperature at 72°30′N; (d) salinity at 72°30′N; (e) temperature at 71°30′N; (f) salinity at 71°30′N. Solid lines represent observations and simulations with data assimilation, broken lines represent free simulations. Observation averages are black, TOPAZ is blue, NEMO is red, and ROMS is pink. (For interpretation of the references to colour in this figure legend, the reader is referred to the web version of this article.)

the *T-S* diagram (Fig. 9). NEMO-F has too low densities, whereas NEMO-A and both TOPAZ simulations have densities within observed values but with less variation throughout the water column. ROMS resembles the observations but with density-compensating fresh and cold biases. During summer, both TOPAZ and NEMO simulations show steeper temperature profiles below the thermocline (i.e., too weak gradients), whereas ROMS compares well with the observed average temperature profile (Supplementary Fig. S4). Similar to the southernmost station, the thermocline and halocline both become deeper (more realistic) but also weaker than observed in TOPAZ-A as compared with TOPAZ-F. NEMO-A shows the least salinity bias below the halocline, although ROMS has a sub-halocline salinity profile slope that is closer to the observations.

In the frontal area between water of Atlantic and Arctic origin at the northernmost location, all the simulations are within the observed variability both in terms of temperature and salinity (Fig. 8). All simulations, to a varying degree, resemble the observed pattern of both temperature and salinity decreasing with depth, although the haline contribution to the stratification is less in the simulations compared with the observations. However, the shallower bottom depth in the NEMO and TOPAZ models at this location may partly explain the discrepancy. In terms of density, all simulations are within the observed density range, although with different modelled density ranges (Fig. 9). None of the models represent the surface water due to a cold bias in upper water temperature, while the aforementioned shallower bottom depth possibly explains the lack of dense water near the bottom in TOPAZ-A and both NEMO simulations. The summer conditions at the northernmost station are similar to the stations further south (Supplementary Fig. S4, S5). There is a strong stratification in the upper 100 m, which is present in all model simulations, except for only a very weak thermal stratification in TOPAZ-A. The closest agreement with the observed temperature profile is found in NEMO-A, while also ROMS reproduces a similar temperature profile except for a cold bias. In terms of salinity, the assimilation again produces a shift towards more saline conditions in NEMO-A as compared to NEMO-F, with NEMO-A displaying close to the observed salinity below the thermocline while being too saline in the upper mixed layer. Again in TOPAZ, the assimilation tends to weaken both the thermocline and the halocline.

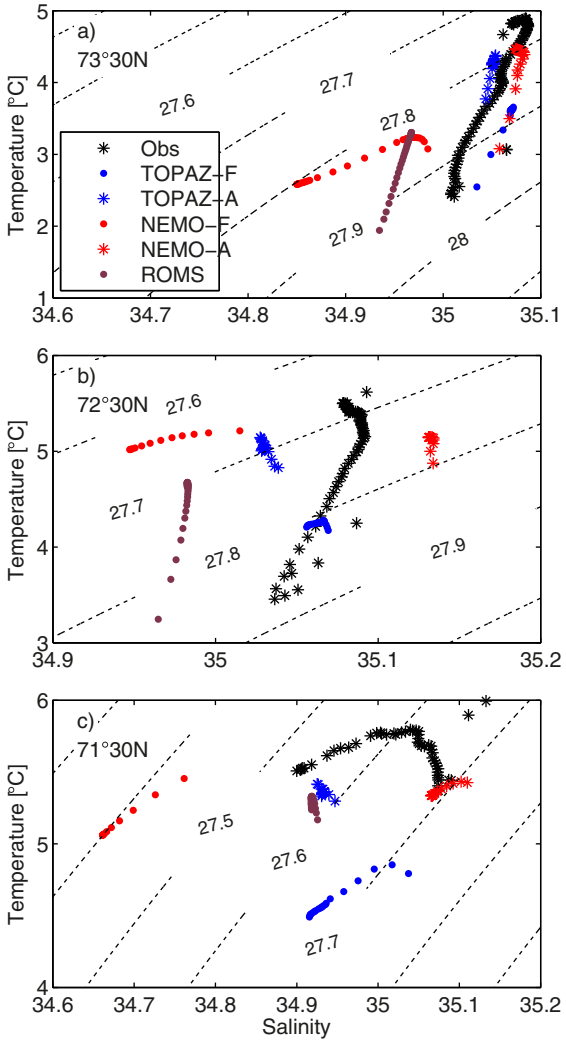


**Fig. 9.** *T-S* diagrams based on the average profiles shown in Fig. 8 (March 1993–2009). (a) 73°30'N; (b) 72°30'N; (c) 71°30'N. Dots represent free simulations; stars represent observations and simulations with data assimilation.

Observations show that the eastward flow of AW consists of one and occasionally two branches, with the main branch located approximately at 72°30'N (Ingvaldsen et al., 2002; Skagseth et al., 2008). In the south, the Norwegian Coastal Current is hugging the coast (Skagseth et al., 2011). A bottom-intensified westward flow of Polar Water follows along the northern slope of the Bear Island Trough, intermittently interrupted by eastward flow of AW and a subsequent upslope displacement of the Polar Front (Lien et al., 2013b). The modelled current structure through the BSO show some similarities, but also some differences both compared to observations and between the different models (Figs. 6 and 7). In both the simulations using TOPAZ, the main AW inflow branch is located at 73°N, while another main branch is located in the frontal area between the AW and the coastal water, i.e., partly outside the sub-section defined by the extent of the mooring array. This southern inflow branch is mostly too fresh to be defined as AW if we use the common criterion $S > 35$ in addition to the temperature criterion to define AW. Adding a salinity criterion is necessary to discriminate between AW and coastal water masses when the section is extended southwards. Also in TOPAZ, there is another inflow branch carrying a mixture of AW and Polar waters eastward along the northern slope of the BSO. In the NEMO simulations, a main inflow branch is located between 72°30'N and 73°N. This inflow is stronger in NEMO-F than in NEMO-A. ROMS exhibits two inflow branches located between 72°30'N and 73°30'N, in addition to a third branch at 72°N, while a coastal current is located in the southernmost part of the section. A bottom-intensified outflow in the deepest part of the section is present in all the simulations.

#### 3.1.3. Adjusted volume and heat transports

Based on the above findings, we re-calculate the modelled volume and heat transports by extending the section to include the full BSO and adjusting the AW definition according to the individually modelled temperature biases and by adding a salinity criterion ($S > 35.0$) subsequently adjusted for the individual model biases. The largest change in the volume transport is seen in NEMO, with an increase of 1 Sv in both simulations (Table 4; Supplementary Fig. S6). The volume transport is reduced by 0.2 Sv in ROMS, while there are only minor differences in TOPAZ. Hence, the part of the section not occupied by the mooring array contains a substantial part of the AW inflow in NEMO, whereas in ROMS, that area contributes with an average net westward flow of AW. Similar results are found for the heat transports (Table 5).

### 3.2. Færøy–Shetland Channel

#### 3.2.1. Volume and heat transports

All the simulations capture the seasonal variation in volume transport at 99% confidence (ROMS at 95%; Table 6; Supplementary Fig. S7). In terms of long term average, all the simulations have lower volume transports than the 2.7 Sv estimated by Berx et al. (2013). However, ROMS (2.4 Sv) is within the observed 0.5 Sv uncertainty range. Despite the generally lower modelled volume transports, the variation in NEMO is comparable to the observed variations in terms of standard deviation. ROMS has a substantially larger standard deviation (2.2 Sv) than observed, while TOPAZ has a lower standard deviation.

The observations show a positive trend of 0.002 Sv/year, whereas the TOPAZ and NEMO simulations have trends that are an order of magnitude larger. ROMS has a trend that is similar to the observations in magnitude but with opposite sign.

The correlation between the modelled and observed volume transports in all five model simulations are rather low, yet significant at a 99% confidence level (Table 6; Supplementary Fig. S8).

The average net AW heat transport through the FSC is estimated to 107 TW for the period 1994–2011 (Berx et al., 2013). The corresponding modelled heat transports (1993–2009) are 59 and 64 TW in TOPAZ-F and TOPAZ-A, respectively, 79 and 68 TW in NEMO-F and NEMO-A, respectively, and 89 TW in ROMS (Table 5), thus reflecting the generally lower volume transports.

#### 3.2.2. Hydrography and current structure

The seasonal temperature variation is well captured in all the model simulations with correlations significant to the 99% level (ROMS at 95% significance), whereas the salinity seasonal variation is only significantly captured in TOPAZ-A and NEMO-A (Table 6). For the long term average, we find that both TOPAZ simulations have a warm bias (but strongly reduced in TOPAZ-A), while both the NEMO simulations and ROMS have a cold bias. The largest bias is found in ROMS (−1.30). For salinity, all the model simulations, except NEMO-F, have a fresh bias. The smallest biases are found in NEMO-F (0.01) and TOPAZ-F (−0.03), while the largest bias is found in ROMS (−0.14). All the model simulations have temperature trends that are higher than the observed trend of 0.039 °C/year, spanning the range 0.046 °C/year (NEMO-F) to 0.063 °C/year (TOPAZ-A). For salinity, both simulations using

TOPAZ, as well as NEMO-A have trends of similar magnitude as observed, although TOPAZ-F has negative trend, whereas NEMO-F has a significantly smaller trend and ROMS has a significantly larger trend.

All the simulations, except ROMS, are statistically significantly correlated with the temperature observations, with the highest correlation found in TOPAZ-A ($R = 0.46$). For salinity, the correlations are generally lower than for temperature, and both ROMS and TOPAZ-F have non-significant correlations (Table 6).

All the model simulations resemble the main hydrographic features in the FSC, including AW flowing northward along the Shetland slope with a tilted (shallower in the west) transition zone between the AW and the underlying colder and less saline water masses at a depth of approximately 500–600 m (Supplementary Figs. S9, S10).

The current structure reveals some differences between the models and the observations and also between the different models (Supplementary Figs. S9, S10). The NEMO simulations have a clearly defined current located at the shelf break, consistent with observations, whereas the TOPAZ simulations have a more homogenously distributed flow pattern throughout the section. ROMS has the strongest current speed, with a long-term average in excess of 30 cm/s in the upper 200 m, exceeding the long-term average of $>$ 20 cm/s found in observations (Berx et al., 2013). All the model simulations show, although to a different extent, southward flow below the AW layer, in agreement with observations (Berx et al., 2013).

#### 3.2.3. Bias-adjusted volume and heat transports

The modelled net AW volume and heat transports through the FSC are only slightly changed when the biases in modelled temperature and salinity is taken into account when defining the AW (Table 7). The exception is a decrease from 2.4 Sv to 2.0 Sv in ROMS. For heat transport, there are only small changes also in ROMS. Also, the correlations between the models and the observations remain similar when using the bias-adjusted volume transports.

### 3.3. Færøy North

#### 3.3.1. Volume and heat transports

None of the model simulations are significantly correlated with the observations in terms of volume transport seasonal variations in the FN section (Table 8; Supplementary Fig. S11). Moreover, all the simulations have smaller amplitudes in the seasonal variation compared with the observations. Thus, the models lack some of the fundamental drivers for the seasonal variation in the AW flow along the northern Færøy slope. Obviously, the assimilation is not sufficient to fully overcome these shortcomings.

The long-term average AW volume transport through the FN section is 3.5 Sv with a standard deviation of 0.8 Sv (Supplementary Fig. S12). All the model simulations have lower volume transports compared with the observations. In both NEMO and TOPAZ, the volume transports are larger in the free simulations (3.0 Sv and 1.9 Sv, respectively) compared to the assimilated simulations (2.3 Sv and 1.5 Sv, respectively; Table 8). However, the modelled variability is comparable to the observations in terms of standard deviation. Relatively speaking, the modelled heat transports are lower than the observations compared with the volume transports, which indicate that all the simulations also have a cold bias. The observations show a negative trend in the volume transports of −0.007 Sv/year. All model simulations show larger trends and only NEMO-F has a negative trend (−0.029 Sv/year). The largest trend is found in ROMS (0.102 Sv/year). The correlations between modelled and observed volume transports are non-significant for all the simulations, except NEMO-A ($R = 0.36$; $p < 0.01$) and ROMS ($R = 0.19$; $p < 0.05$).

#### 3.3.2. Hydrography and current structure

Both the TOPAZ and the NEMO simulations closely resemble the observed hydrographic features in the FN section, which is dominated by AW hugging the upper slope and separated from the Norwegian Sea waters by a wedge-shaped front (Supplementary Figs. S13, S14; Østerhus et al., 2005). There is a tendency that the AW extends further into the Norwegian Sea in the free simulations than the assimilated simulations, which partly explains the higher AW volume transports in the free simulations. In ROMS, the front is too steep, which indicates too little lateral mixing and too strong topographical control of the AW flow.

### 3.4. Svinøy Northwest

#### 3.4.1. Volume and heat transports

As noted above, we limit our model section to the west by the 1000 m isobath to only include the eastern branch of the Norwegian Atlantic Current. Only the TOPAZ simulations show significant (99%) correlations with the observed seasonal cycle in volume transport (Table 9; Supplementary Fig. S15). In terms of heat transport, also NEMO-F and ROMS are significantly correlated with the observed seasonal cycle, but at 95% confidence. The long-term average AW volume transport is estimated to 4.4 Sv, based on the approach using a single current meter only, as proposed by Orvik and Skagseth (2003). TOPAZ-F and TOPAZ-A have the smallest volume transports (0.6 Sv and 1.4 Sv, respectively), while the corresponding numbers in NEMO-F and NEMO-A are 2.2 Sv and 2.3 Sv, respectively (Table 8; Supplementary Fig. S16). ROMS has the largest volume transport both in terms of average (2.8 Sv) and variability represented by the standard deviation (2.0 Sv). The observed standard deviation is 1.0 Sv.

TOPAZ-A has a volume transport trend similar to the observations, while the NEMO-A has a higher trend compared with observations and NEMO-F has a similar but negative trend. ROMS has a trend in the volume transport which is almost an order of magnitude larger than the observed trend. In terms of heat transport, the trend is on the low side in both TOPAZ simulations, whereas NEMO-A has a trend similar to the observations. The trend in heat transport in ROMS is approximately twice that observed.

The correlations between the modelled and observed volume transports are low, although significant to 99% confidence level in all simulations. The highest correlation is found in TOPAZ-A and NEMO-A with $R = 0.55$ and $R = 0.54$, respectively. Similar correlations are found for the heat transports (Table 9).

#### 3.4.2. Hydrography and current structure

Both the TOPAZ and NEMO simulations resemble the observed hydrographic patterns in the SNW section, with the AW core located at the shelf break and AW extending westward into the Norwegian Sea. In ROMS, the AW is too constrained by topographic steering (Supplementary Figs. S17–S20). The coastal current is present in all model simulations, but it is more saline in both TOPAZ-A and NEMO-A as compared with both the observations and the free simulations, especially during winter (March).

Looking at the hydrography in more detail, Supplementary Figs. S21–S24 display the vertical profiles and corresponding *T-S* relations for three selected stations representing the shelf, shelf break and shelf slope. NEMO-F resembles the observations most closely at the shelf during winter, whereas the assimilation tends to decrease the stratification at the shelf in both TOPAZ-A (winter only) and NEMO-A, especially in terms of temperature (Supplementary Fig. S21). By contrast, during summer, the inclusion of assimilation improves the vertical temperature gradient at the shelf in TOPAZ

(Supplementary Fig. S23). At the deeper stations, TOPAZ-A and NEMO-A again seem to have excessive vertical mixing in the upper layer, while the assimilation tends to improve the water mass characteristics deeper below, especially at the interface between the AW and the Norwegian Sea Intermediate Water where the assimilation helps decreasing the depth of this interface towards observed values. Within the AW layer, both NEMO and TOPAZ tend to have too little vertical stratification, i.e., too steep slopes of the temperature and salinity vertical profiles. Interestingly, ROMS is generally in better agreement with the vertical gradients in temperature and salinity within the AW layer. However, ROMS is clearly suffering from excessive vertical mixing manifested by too cold and fresh AW and too warm and saline Norwegian Sea Intermediate Water. A likely source of the enhanced mixing is artificial diapycnal mixing associated with the use of sigma coordinates over sloping bathymetry (Marchesiello et al., 2009).

TOPAZ lacks a clearly defined core and the AW flow is too weak and concentrated within the coastal-influenced water at the shelf (Supplementary Figs. S17–S20). However, there are indications of a western branch located approximately at the 2000 m isobaths (not shown), in agreement with observations (e.g., Orvik et al., 2001). In NEMO, the core of the AW current is located at the shelf break, but with lower current speeds than in the observations, resulting in lower than observed AW volume and heat transports.

### 3.5. Fram Strait

#### 3.5.1. Volume and heat transports

A net northward volume transport of 3.0 +/− 0.2 Sv of water masses with $T > 2$ °C has been reported by Beszczynska-Möller et al., 2012 for the period 1997–2010. Using a similar criterion for AW and the period 1993–2009, we find the following volume transports based on the model results: 1.5 Sv and 1.2 Sv in TOPAZ-F and TOPAZ-A, respectively, 2.3 Sv and 2.0 Sv in NEMO-F and NEMO-A, respectively, and 1.4 Sv in ROMS. For a comparison with observed heat transport, we refer to Schauer et al., 2004, who reported a net northward heat transport of 16 +/− 12 TW and 41 +/− 5 TW for the years 1997/98 and 1998/99, respectively, using $T > 1$ °C to define AW. Corresponding values for modelled heat transports during the full period 1993–2009 are 21 TW and 15 TW for TOPAZ-F and TOPAZ-A, respectively, 28 TW and 24 TW in NEMO-F and NEMO-A, respectively, and 21 TW in ROMS. Thus, modelled values are within the range reported for the two-year period 1997–1999. Note also that the recirculation of AW within the Fram Strait adds to the uncertainty in the transport estimates. The model-based estimates include the full section and therefore any recirculation will reduce the net transport.

#### 3.5.2. Hydrography and current structure

The 2-degree isotherm used to define AW in the Fram Strait is located between the surface and approximately 500 m depth on the Svalbard slope, and extending towards 2°W (Fig. 2 in Beszczynska-Möller et al., 2012). Additionally, a core of recirculating AW has been observed at 3°W (Beszczynska-Möller et al., 2012). The TOPAZ-F and NEMO-F both agrees well with the observations in terms of the westward extension of the AW layer (Supplementary Fig. S25), although the depth of the 2-degree isotherm is deeper in the models compared with the observations at the shelf slope. In TOPAZ-A and NEMO-A, the AW layer only extends to about 4°E. In ROMS, the extent of AW in excess of 2 °C is limited to the narrow West Spitsbergen Current core located upslope. The AW recirculating in the central and western parts of the section is generally colder in the assimilated simulations compared with the free simulations. In ROMS, the temperature is generally on the low side throughout the section.

The current structure varies considerably between the models. The West Spitsbergen Current is well-defined in both NEMO and the ROMS simulations, along with the southward flowing East Greenland Current along the Greenland slope. In TOPAZ, the West Spitsbergen Current is almost indiscernible, while the East Greenland Current is well defined. The strongest current speed in the West Spitsbergen Current is found in ROMS, exceeding 20 cm/s in the core, which is close to the observed long-term average current speed (Beszczynska-Möller et al., 2012). The East Greenland Current extends towards the bottom and is located between 1°W and the Greenland shelf, with the core located near the surface between 4°W and 3°W (Beszczynska-Möller et al., 2012). All model simulations, except ROMS (1°W–1°E), agrees well with the observations in terms of position of the deep East Greenland Current. However, only ROMS shows current speeds comparable with the observations for the below-pycnocline part of the current.

## 4. Discussion

Five model hindcast simulations are evaluated in terms of hydrography and ocean transports in the Nordic Seas as inferred from repeatedly sampled sections. Two of the model simulations (TOPAZ-A and NEMO-A) include data assimilation and are currently used operationally in forecast mode through the Copernicus Marine Service. Additionally, simulations with these two models in a non-assimilating mode, as well as a third, non-assimilating model (ROMS) are included in our comparison. The purpose of the study is to provide a first-step model-data and model inter-comparison that identifies possible differences in model performance with respect to some key parameters of importance both for the individual model development, the coordination of the modelling efforts in the ocean science community, and for the users of ocean model results.

### 4.1. Challenges when comparing observations with model results

A model evaluation based on comparison with observations is not straightforward. In this analysis, we compare ocean transports of water masses defined by specific hydrographic properties, as well as geographically-dependent hydrographic time series. The former is prone to hydrographic biases in the model, whereas the latter is prone to differences in geographical position of ocean currents and fronts, arising from, among other things, issues related to spatial resolution and differences between real-world and model bathymetry. Here, we propose a way to overcome some of these challenges by utilizing a two-step analysis, as presented for the BSO and FSC. First, we perform a straightforward comparison between observed and modelled ocean transports using similar geographic and hydrographic bounds as used when calculating observation-based estimates. Then, we use the hydrographic time series to calculate model biases, which in turn are used to adjust the applied water mass definition before re-calculating the modelled ocean transports. Thus, we have reduced the influence of model bias in temperature and salinity on the water mass definitions, although the error arising from the geographical dependence of the hydrographic time series are still retained.

In the FSC, we use the maximum salinity and corresponding temperature, which is geographically independent, whereas in the BSO, an inspection of the vertical section plots shows that the AW core is in fact located within the geographical boundaries applied when calculating the hydrographic properties. Moreover, we include the full BSO in our second-step calculation of modelled ocean transports, and thus also remove the geographical dependencies. However, this comes at the cost of making the comparison with observations less accurate. Expanding on this compromise, it is important to note that also the observations contain errors and

uncertainty, arising from their limited geographical extent and/or spatial resolution. In the BSO, the horizontal sampling resolution is approximately 50 km (Ingvaldsen et al., 2002), which is an order of magnitude larger than the internal radius of deformation (Nurser and Bacon, 2014). In addition, the measurements are bounded by 71°30'N and 73°30'N, and thus do not fully account for variations in the width of the AW inflow (Ingvaldsen, 2005). In the FSC, the transport time series consist of data from various observation platforms at differing positions that are merged into one composite time series. Thus, the observations and the models may capture spatiotemporal variability differently.

Examples of discrepancies between the models and the observations, possibly due to incomplete observational datasets, include the modelled BSO inflow maxima during the winters 1999/00 and 2004/05 when no concurrent maximum is seen in the observations with regard to the former peak, while the latter maximum (2004/05) was investigated by Lien et al. (2013b), who proposed a mechanism for transient increases in the AW flow through the BSO outside the monitoring array. Similarly, the most prominent peak in the observed AW flow through the BSO (winter 2005/06) is only to some degree captured in the model simulations. These findings call for further efforts in identifying the mechanisms for spatiotemporal variability in the BSO throughflow.

The present study compares two regional model simulations (TOPAZ and ROMS) with a global simulation (NEMO). A regional model allows for higher spatial resolution, as well as more area-specific parameterizations of sub-gridscale processes. However, these advantages come with the cost of relying on lateral boundary conditions. Thus, the outer, typically coarser resolution model, to a varying degree influences the solution of the inner model simulation, whereas in a global model all processes are handled internally. In this specific case, the ROMS model simulation relies on monthly values for the physical parameters, such as $T$ and $S$, from the coarser SODA simulation (Carton and Giese, 2008) in the North Atlantic, whereas TOPAZ has its southern boundary in the South Atlantic and therefore solves the Atlantic–Nordic Seas exchanges internally. This may explain the relatively low score in ROMS in the FSC section.

### 4.2. Added value from data assimilation

The hydrographic observations used in the above analysis are also included in the data assimilation. Thus, the results from the simulations using data assimilation and the observations have inherent dependencies, and therefore improvements such as reduced biases and especially improved water column structure are to be expected. Also, the ROMS simulation applies sea surface salinity restoration towards monthly averages from the SODA re-analysis (Carton and Giese, 2008). Thus, the ROMS salinities are, to some degree, forced to vary in phase with observed salinity.

Our comparison between the free and the data assimilating simulations reveals only a limited added-value by the inclusion of hydrographical data assimilation. Based on the two sections BSO and FSC, we find that hydrographic biases are sometimes reduced and sometimes increased, although there is a tendency that relatively large biases are reduced when observations are assimilated. Adding to that, we find that biases in temperature, although reduced, tend to persist despite the inclusion of data assimilation. One possible explanation for this is a limited amount of data being available for the assimilation. Looking more specifically at vertical profiles of temperature and salinity at selected stations in the SNW and the BSO, we find that the inclusion of assimilation generally improves the vertical hydrographic structure.

The inclusion of ocean transport data in the analysis adds an independent measure of model performance and thereby also an independent evaluation of the value added by the assimilation. Interestingly, the inclusion of data assimilation only offers limited improvements in terms of volume and heat transports and sometimes even acts to deteriorate the ocean transports (e.g., in the FN section), even though the sea surface height, which represents the barotropic forcing of the ocean currents is assimilated. Actually, the closest overall agreement between modelled and observed ocean transports through the BSO is found in the ROMS model, whereas TOPAZ and NEMO are underestimating and overestimating, respectively, the transports to the Barents Sea (Table 3). Because the oceanic heat transport to the Barents Sea affects the sea–ice extent on inter-annual to decadal timescales (Årthun et al., 2012), we expect that assimilation of sea ice is needed to maintain a realistic long-term average sea-ice extent in both NEMO and TOPAZ.

We identify a general improvement in the performance in the simulations using data assimilation over the free simulations, especially for the TOPAZ model (Table 10). The data assimilation increases the performance of TOPAZ in 4 out of 4 sections investigated, while it increases the performance of the NEMO model in 3 out of 4 sections, of which 2 sections show only minor overall improvements. A similar result is found when looking at individual parameters (Table 10).

Focusing on individual sections and parameters, we note that only one of the models (TOPAZ-A) performs best on more than one section (FSC and SNW), whereas only NEMO-A performs best on more than one parameter ($S$, $V$ and $Q$). Focusing on individual models, for example for the BSO (Table 10), TOPAZ has a tendency of performing better on hydrographic properties compared to ocean transports, whereas ROMS performs equally well on both, outperforming TOPAZ on transports. This latter result is not surprising, as the higher spatial resolution in ROMS is likely more advantageous in terms of dynamical processes as compared with processes important for the hydrographic properties, such as ocean-atmosphere heat fluxes and freshwater fluxes. Summarized, ROMS has a score that is lower or comparable to the free TOPAZ and NEMO simulations, whereas the assimilated TOPAZ and NEMO simulations perform equally well overall.

The main results of our analysis illustrate the complexity of several factors contributing to the difference in model skill depending on region and dominating processes. As an example, ROMS, which is the only model with tides included and that has the highest resolution in the horizontal and within shallow areas also in the vertical, shows the highest score in the BSO where both the atmospheric and tidal forcing is strong. Here, the increased resolution in both the ocean and the atmospheric forcing, which allows for the governing processes to be better resolved and represented, can be as valuable as the inclusion of data assimilation in a coarser-resolution model. In the SNW section, however, where basin-shelf interaction over steep topography plays an important role TOPAZ shows the highest score. Here, ROMS falls short because the steep topography gives ROMS and its terrain-following vertical coordinate a disadvantage due to its' proneness to internal-pressure gradient errors (e.g., Haney, 1991) and diapycnal diffusion (e.g., Marchesiello et al., 2009). Thus, it may be impossible to single out one universally superior model. Rather, carefully assessing dominating features and processes specific to the region of interest and subsequently choosing adequate model and set-up is necessary. In principle, high resolution should not replace data assimilation or vice versa. Higher resolution increases the model sensitivity to the forcing, and thus, will improve the skills of variables that are more or less directly related to the forcing. Data assimilation in coarse resolution models may compensate for the lack of sensitivity, but may also aggravate the skills if not applied properly. Data assimilation has the advantage that it can improve the skills of variables that are less directly related to the forcing. The improved skills of the simulations including data assimilation investigated here show that the assimilation was successful, and the

relative status quo of the three different models can be explained by the indirect relationship between the model forcings and the observations used for validation.

## 5. Concluding remarks

Often, the numerical ocean model results themselves are not the end product sought, but rather represent the foundation for higher-complexity models, such as ecosystem models. However, different applications put different requirements on the model performance. Examples include Lagrangian trajectory models for fish eggs and larvae and oil spills (e.g., Vikebø et al., 2014, 2015), which put strong constraints on the quality of the modelled currents and transports, whereas modelling the basin wide distribution, migration and life cycle of higher trophic level species such as herring, blue whiting or mackerel (e.g. Utne et al., 2012), require realistic hydrographic properties throughout the Norwegian Sea basins. Based on the above results, we find that the ROMS model is a viable option for Lagrangian trajectory simulations, due to its strong performance in terms of currents and transports, whereas both TOPAZ and NEMO are better options when the quality of the basin-wide hydrography becomes important, due to the added value from the assimilation of hydrographic observations.

## Acknowledgement

This work was supported by the EU within the projects MyOcean2 (grant number 283367), MyOcean FollowOn (grant number 633085) and Copernicus Marine Environmental Monitoring Service. A grant of CPU time (nn2993k) from the NOTUR2 Norwegian supercomputing project has been used for the TOPAZ simulations. Bogi Hansen, Kjell Arild Orvik and Randi Ingvaldsen are acknowledged for help in preparing the observation data from the fixed sections. We thank Karen Gjertsen for preparing Fig. 1.

## Supplementary materials

Supplementary material associated with this article can be found, in the online version, at doi:10.1016/j.ocemod.2015.12.010.

## References

Aagaard, K., Greisman, P., 1975. Toward new mass and heat budgets for the Arctic Ocean. J. Geophys. Res. 80, 3821–3827.
Årthun, M., Eldevik, T., Smedsrud, L.H., Skagseth, Ø., Ingvaldsen, R.B., 2012. Quantifying the influence of Atlantic heat on Barents Sea ice variability and retreat. J. Climate 25, 4736–4743.
Beaugrand, G., Luczak, C., Edwards, M., 2009. Rapid biogeographical plankton shifts in the North Atlantic Ocean. Glob. Change Biol. 15, 1790–1803.
Berx, B., Hansen, B., Østerhus, S., Larsen, K.M., Sherwin, T., Jochumsen, K., 2013. Combining in situ measurements and altimetry to estimate volume, heat and salt transport variability through the Færøy–Shetland Channel. Ocean Sci 9, 639–654.
Beszczynzka-Möller, A., Fahrbach, E., Schauer, U., Hansen, E., 2012. Variability in Atlantic water temperature and transport at the entrance to the Arctic Ocean, 1997-2010. ICES J. Mar. Sci. 69 (5), 852–863.
Bleck, R., 2002. An oceanic general circulation model framed in hybrid isopycnic-Cartesian coordinates. Ocean Modell 4, 55–88.
Blindheim, J., Loeng, H., 1981. On the variability of Atlantic influence in the Norwegian and Barents Seas. Fiskeridir. Skrev. Ser. Hav. 17, 161–189.
Blindheim, J., Østerhus, S., 2003. The Nordic Seas, main oceanographic features. In: Drange, H., Dokken, T., Furevik, T., Gerdes, R., Berger, W. (Eds.), The Nordic Seas: An Integrated Perspective, 158. Amer. Geophys. Union Mono. Ser., pp. 11–37.
Budgell, W.P., 2005. Numerical simulation of ice-ocean variability in the Barents Sea region – towards dynamical downscaling. Ocean Dynam 55, 370–387.
Carton, J.A., Giese, B.S., 2008. A reanalysis of ocean climate using Simple Ocean Data Assimilation (SODA). Mon. Weather Rev. 136, 2999–3017.
Dee, D.P., Co-authors, 2011. The ERA-interim reanalysis: configuration and performance of the data assimilation system. Q. J. Roy. Meteor. Soc. 137, 553–597.
Eldevik, T., Nilsen, J.E.Ø., 2013. The Arctic–Atlantic thermohaline circulation. J. Climate 26, 8698–8705.
Ferry, N., Parent, L., Garric, G., Bricaud, C., Testut, C.E., Le Galloudec, O., Lellouche, J.M., Drevillon, M., Greiner, E., Barnier, B., Molines, J.M., Jourdain, N.C., Guinehut, S., Cabanes, C., Zawadzki, L., 2012. GLORYS2V1 global ocean reanalysis of the altimetric era (1992–2009) at meso scale. Mercator Newsl. 44, 28–39.
Gerber, F., Sedlacek, J., Knutti, R., 2014. Influence of the western North Atlantic and the Barents Sea on European winter climate. Geophys. Res. Lett. 41. doi:10.1002/2013GL058778.
Häkkinen, S., Mellor, G.L., 1992. Modelling the seasonal variability of a coupled arctic ice–ocean system. J. Geophys. Res. 97, 20285–20304.
Haney, R.L., 1991. On the pressure gradient force over steep topography in sigma coordinate ocean models. J. Phys. Oceanogr. 21, 610–619.
Hansen, B., Østerhus, S., 2000. North Atlantic – Nordic Seas exchanges. Prog. Oceanogr. 45, 109–208.
Hauge, K.H., Blanchard, A., Andersen, G., Boland, R., Grøsvik, B.E., Howell, D., Meier, S., Olsen, E., Vikebø, F., 2014. Inadequate risk assessments – A study on worst-case scenarios related to petroleum exploitation in the Lofoten area. Mar. Policy. 44, 82–89.
Hunke, E.C., Dukowicz, J.K., 1997. An elastic-viscous-plastic model for sea ice dynamics. J. Phys. Oceanogr. 27, 1849–1867.
Ingvaldsen, R., 2005. Width of the North Cape current and location of the Polar front in the western Barents Sea. Geophys. Res. Lett. 32, L16603.
Ingvaldsen, R., Loeng, H., Asplin, L., 2002. Variability in the Atlantic inflow to the Barents Sea based on a one-year time series from moored current meters. Cont. Shelf Res. 22, 505–519.
Ivanov, V.V., Shapiro, G.I., 2005. Formation of a dense water cascade in the marginal ice zone in the Barents Sea. Deep-Sea Res. Part I. 52, 1699–1717.
Jónsson, S., Valdimarsson, H., 2012. Water mass transport variability to the North Icelandic shelf, 1994-2010. ICES J. Mar. Sci. 69, 809–815.
Lellouche, J.-M., Le Galloudec, O., Drévillon, M., Régnier, C., Greiner, E., Garric, G., Ferry, N., Desportes, C., Testut, C.-E., Bricaud, C., Bourdallé-Badie, R., Tranchant, B., Benkiran, M., Drillet, Y., Daudin, A., de Nicola, C., 2013. Evaluation of real time and future global monitoring and forecasting systems at Mercator Océan. Ocean Sci. Disc. 9 (2), 1123–1185.
Lien, V.S., Gusdal, Y., Vikebø, F.B., 2014. Along-shelf hydrographic anomalies in the Nordic Seas (1960–2011): locally generated or advective signals? Ocean Dyn. 64, 1047–1059.
Lien, V.S., Gusdal, Y., Albretsen, J., Melsom, A., Vikebø, F.B., 2013a. Evaluation of a Nordic Seas 4 km numerical ocean model hindcast archive (SVIM), 1960–2011. Fisken og Havet 7, 82.
Lien, V.S., Vikebø, F.B., Skagseth, Ø., 2013b. One mechanism contributing to co-variability of the Atlantic inflow branches to the Arctic. Nature Commun 4, 1488.
Madec, G., and the NEMO team., 2008. NEMO ocean engine. Note du Pôle de modélisation, Institut Pierre-Simon Laplace (IPSL), France, No. 27 ISSN, 1288–1619, 2008.
Marchesiello, P., Debreu, L., Couvelard, X., 2009. Spurious diapycnal mixing in terrain-following coordinate models: the problem and a solution. Ocean Modell 26, 156–169.
Mauritzen, C., Hansen, E., Andersson, M., Berx, B., Beszczynzka-Möller, A., Burud, I., Christensen, K.H., Debernard, J., de Steur, L., Dodd, P., Gerland, S., Godøy, Ø., Hansen, B., Hudson, S., Høydalsvik, F., Ingvaldsen, R., Isachsen, P.E., Kasajima, Y., Koszalka, I., Kovacs, K.M., Koltzow, M., LaCasce, J., Lee, C.M., Lavergne, T., Lydersen, C., Nicolaus, M., Nilsen, F., Nøst, O.A., Orvik, K.A., Reigstad, M., Schyberg, H., Seuthe, L., Skagseth, Ø., Skardhamar, J., Skogseth, R., Sperrevik, A., Svensen, C., Søiland, H., Teigen, S.H., Tverberg, V., Riser, C.W., 2011. Closing the loop – approaches to monitoring the state of the Arctic Mediterranean during the International Polar Year 2007–2008. Prog. Oceanogr. 90, 62–89.
Mellor, G.L., Kantha, L., 1989. An ice-ocean coupled model. J. Geophys. Res. 94, 10937–10954.
Nurser, A.J.G., Bacon, S., 2014. The Rossby radius in the Arctic Ocean. Ocean Sci 10, 967–975.
Orvik, K.A., Skagseth, Ø., 2005. Heat flux variations in the eastern Norwegian Atlantic current toward the Arctic from moored instruments, 1995–2005. Geophys. Res. Lett. 32 (14), L14610.
Orvik, K.A., Skagseth, Ø., 2003. Monitoring the Norwegian Atlantic slope current using a single moored current meter. Cont. Shelf Res. 23, 159–176.
Orvik, K.A., Skagseth, Ø., Mork, M., 2001. Atlantic inflow to the Nordic Seas: current structure and volume fluxes from moored current meters, VM-ADCP and SeaSoar-CTD observations, 1996-1999. Deep-Sea Res. Part I. 48, 937–957.
Østerhus, S., Turrell, W.R., Jónsson, S., Hansen, B., 2005. Measured volume, heat, and salt fluxes from the Atlantic to the Arctic Mediterranean. Geophys. Res. Lett. 32 (7), L07603.
Ottersen, G., Stige, L.C., Durant, J.M., Chan, K.S., Rouyer, T.A., Drinkwater, K.F., Stenseth, N.C., 2013. Temporal shifts in recruitment dynamics of North Atlantic fish stocks: effects of spawning stock and temperature. Mar. Ecol.-Prog. Ser. 480, 205–225.
Payne, M.R., Hatfield, E.M.C., Dickey-Collas, M., Falkenhaug, T., Gallego, A., Groger, J., Licandro, P., Llope, M., Munk, P., Rockmann, C., Schmidt, J.O., Nash, R.D.M., 2009. Recruitment in a changing environment: the 2000 s North Sea herring recruitment failure. ICES J. Mar. Sci. 66, 272–277.
Reistad, M., Breivik, Ø., Haakenstad, H., Aarnes, O.J., Furevik, B.R., Bidlot, J.R., 2011. A high resolution hindcast of wind and waves for the North Sea, the Norwegian Sea, and the Barents Sea. J. Geophys. Res. 116, C05019.
Reynolds, R.W., Smith, T.M., Liu, C., Chelton, D.B., Casey, K.S., Schlax, M.G., 2007. Daily high-resolution blended analyses for sea surface temperature. J. Clim. 20, 5473–5496.

Sakov, P., Oke, P.R., 2008. A deterministic formulation of the ensemble Kalman filter: an alternative to ensemble square root filters. Tellus A 60, 361–371.
Sakov, P., Counillon, F., Bertino, L., Lisæter, K.A., Oke, P.R., Korablev, A., 2012. TOPAZ4: an ocean-sea ice data assimilation system for the North Atlantic and Arctic. Ocean Sci 8 (4), 633–656.
Schauer, U., Fahrbach, E., Østerhus, S., Rohardt, G., 2004. Arctic warming through the Fram Strait: oceanic heat transport from 3 years of measurements. J. Geophys. Res. 109, C06026.
Segtnan, O.H., Furevik, T., Jenkins, A.D., 2011. Heat and freshwater budgets of the Nordic seas computed from atmospheric reanalysis and ocean observations. J. Geophys. Res 116, C11003.
Shchepetkin, A.F., McWilliams, J.C., 2005. The regional oceanic modeling system (ROMS): a split-explicit, free-surface, topography-following-coordinate oceanic model. Ocean Modell 9, 347–404.
Skagseth, Ø., Drinkwater, K.F., Terrile, E., 2011. Wind- and buoyancy-induced transport of the Norwegian Coastal Current in the Barents Sea. J. Geophys. Res. 116, C08007.
Skagseth, Ø., Furevik, T., Ingvaldsen, R., Loeng, H., Mork, K.A., Orvik, K.A., Ozhigin, V., 2008. Volume and heat transports to the Arctic Ocean via the Norwegian and Barents Seas. In: Dickson, R., Meincke, J., Rhines, P. (Eds.), Arctic Subarctic Ocean Fluxes: Defining the Role of the Northern Seas in Climate. Springer, New York, pp. 45–64.
Smedsrud, L.H., Esau, I., Ingvaldsen, R.B., Eldevik, T., Haugan, P.M., Li, C., Lien, V.S., Olsen, A., Omar, A.M., Otterå, O.H., Risebrobakken, B., Sandø, A.B., Semenov, V.A., Sorokina, S.A., 2013. The role of the Barents Sea in the climate system. Rev. Geophys. 51, 415–449.
Sundby, S., 2000. Recruitment of Atlantic cod stocks in relation to temperature and advection of copepod populations. Sarsia 85, 277–298.
Utne, K.R., Hjøllo, S.S., Huse, G., Skogen, M., 2012. Estimating consumption of Calanus finmarchicus by planktivorous fish in the Norwegian Sea using a fully coupled 3D model system. Mar. Biol. Res. 8, 527–547.
Vikebø, F.B., Rønningen, P., Meier, S., Grøsvik, B.E., Lien, V.S., 2015. Dispersants have limited effects on exposure rates of oil spills on fish eggs and larvae in Shelf Seas. Environ. Sci. Technol. 49, 6061–6069.
Vikebø, F.B., Rønningen, P., Lien, V.S., Meier, S., Reed, M., Ådlandsvik, B., Kristiansen, T., 2014. Spatio-temporal overlap of oil spills and early life stages of fish. ICES J. Mar. Sci. 71, 970–981.